

Deep Wide-Field Spectrophotometry of the Open Cluster M67

Xiaohui Fan

Princeton University Observatory, Princeton, NJ, 08544
and Beijing Astronomical Observatory, Chinese Academy of Sciences,
Beijing, 100080, P.R.China
Email : fan@astro.princeton.edu

David Burstein

Department of Physics and Astronomy, Arizona State University, Tempe, AZ 85287-1504
Email : burstein@samuri.la.asu.edu

Jian-sheng Chen, Jin Zhu, Zhaoji Jiang, Hong Wu,
Haojing Yan, Zhongyuan Zheng, Xu Zhou
Beijing Astronomical Observatory, Chinese Academy of Sciences,
Beijing, 100080, P.R. China
Email : chen,zj,jiang,wu,yhj,zzy,zhouxu@qso.bao.ac.cn

Li-Zhi Fang

Department of Physics, University of Arizona, Tucson, AZ 85721
Email : fanglz@time.physics.arizona.edu

Fuzhen Chen, Zugan Deng, Yaoquan Chu
University of Science and Technology of China, Beijing, 100039, P.R. China

J. J. Hester, Rogier A. Windhorst, Yong Li
Department of Physics and Astronomy, Arizona State University, Tempe, AZ 85287-1504
Email : jjh@wfpc3.la.asu.edu,raw@cosmos.la.asu.edu,li@samuri.la.asu.edu

Phillip Lu

Department of Physics and Astronomy, Western Connecticut State University,
Danbury, CT 06810
Email : lu@wcsu.ctstateu.edu

Wei-Hsin Sun, Wen-Ping Chen, Wean-Shun Tsay, Tzi-Hong Chiueh,
Ting-Chang Lin, Hui-Jean Guo, Yong-Ik Byun
Institute of Astronomy, National Central University, Chung-Li, Taiwan
Email : sun,wchen,tsay,chiueh,lin,batcmgr,byun@phyast.phy.ncu.edu.tw

Received _____; accepted _____

ABSTRACT

We present nine color CCD intermediate-band spectrophotometry of a two square degree field centered on the old open cluster M67, from 3890Å to nearly 1μ . These observations are taken as a part of the BATC (Beijing-Arizona-Taipei-Connecticut) Color Survey of the Sky, for both scientific and calibration reasons. The BATC program uses a dedicated 60/90 cm Schmidt telescope with a 2048×2048 CCD and 15 specially-designed intermediate-band filters to be applied to both galactic and extragalactic studies.

With these data we show that the BATC survey can reach its goal of obtaining spectrophotometry to a zero point accuracy of 0.01 mag, and down to $V = 21$ with 0.3 mag random error. Nine-band spectrophotometry of 6558 stars is presented. Systematic issues studied include the effect of image undersampling, astrometric accuracy and transformation from BATC photometric system to broad-band systems.

We fit the color-magnitude diagrams (CMDs) with Worthey’s theoretical models. The net result is the excellent fit of the 4.0 Gyr, $[\text{Fe}/\text{H}] = -0.10$ model to our data, including a good fit to the main sequence (MS) turn-off. This fit predicts $(m - M)_0 = 9.47 \pm 0.16$ and $E(B-V)$ between 0.015 and 0.052. We show that 16% of stars in M67 are binaries with mass-ratio larger than 0.7. Our data are consistent with a toy model with 50% of the stars in M67 being binaries and a random distribution of binary mass-ratios, although other models with different mass-ratio distributions cannot be ruled out.

The spatial distribution and mass function (MF) of stars in M67 show marked effects of dynamical evolution and evaporation of stars from the cluster. Blue stragglers and binary stars are the most condensed within the cluster, with degree of condensation depending on mass. The inner part of M67 is missing most of

the lower mass MS stars. We find M67 to have an elongated shape, oriented at an angle of 15° relative to the galactic plane.

Within its tidal radius, the observed MF of M67 between $1.2 M_\odot$ and $0.8 M_\odot$ has a Salpeter slope $\eta = -1.93 \pm 0.66$. For stars of mass below $0.8 M_\odot$, $\eta \sim 0$. It is plausible that the leveling-off of the MF at lower masses is a result of evaporation of lower mass stars in this mass range at a rate of one every $\sim 10^7$ years. If so, it is plausible that the IMF of M67 has the canonical field value of $\eta = -2.0$.

Overall, we find the stellar distribution as a function of mass within M67, and the observed MF, are in good agreement with theoretical predictions of dynamical evolution and evaporation of an old galactic cluster. Moreover, the fraction of binary stars and inferred IMF for higher mass main sequence stars for this old galactic cluster are consistent with known field star values. This implies a similarity of IMF that persists for at least 4 Gyr in the disk of our Galaxy.

Subject headings: clusters: galactic — clusters, individual: M67 —
stellar dynamics — initial mass function

1. Introduction

M67 is one of the most-studied old open clusters, because it is reasonably close, populous (~ 1000 stars) and of similar age as the Sun (cf. Janes & Phelps 1994). As such, photometry of its stars ranges from photographic (e.g., Johnson & Sandage 1955, Racine 1971) to CCD (e.g., Gilliland et al. 1991, Montgomery, Marschall & Janes 1993; hereafter MMJ), and from UBVRI (Gilliland et al.; MMJ) to uvby (Nissen, Twarog & Crawford 1987) to DDO (Janes & Smith 1984). The goals of the photometry have been wide ranging. They include establishment of photometric standard stars in the cluster (e.g., Schild 1983, Chevalier & Ilovaisky 1991); determination of cluster age and metallicity (e.g., Gilliland et al.; MMJ; Burstein, Faber & Gonzalez 1986); and determination of the physical properties of the cluster, such as luminosity function (LF), spatial distribution, binary fraction, blue stragglers, and dynamical state of the cluster, etc. (cf. Racine 1971; Francic 1989; MMJ).

In this paper we report a new photometric investigation of M67 that studies this cluster over out to a large radius, $\sim 1^\circ$, and down to faint apparent magnitudes (equivalent of $V \sim 20$). The photometric system we use is new, part of a 15-filter intermediate-band system designed to cover the wavelength range $3300\text{\AA} - 1\mu$, which avoids known bright or variable sky lines (cf. Thuan & Gunn 1976), and is equally applicable to galactic and extragalactic studies.

The M67 observations reported here were obtained both for scientific reasons and as part of the calibrations done for the Beijing-Arizona-Taipei-Connecticut (BATC) Color Survey of the Sky. The BATC survey is a cooperative long term program by the institutions represented by the authors of this paper. The observational goal of the BATC survey is to obtain accurate ($\approx 1\%$) spectrophotometry for all stellar and diffuse objects in 500 one deg^2 areas of the sky centered on nearby spiral galaxies, active galaxies, QSO's and various calibration fields for Galactic and extragalactic objects, as well as random fields at high galactic latitudes. M67

was chosen as one of our first targets specifically because it has been well-studied in the past, and because its large angular size provides data for a number of tests of the BATC Survey CCD+filter+telescope system.

The observations and reduction of the M67 data are described in §2. Special aspects of how BATC data are obtained and reduced are highlighted. In §3, the combination of large field of view with accurate intermediate-band photometry permit us to comprehensively investigate both the photometric and the astrometric accuracy we can attain with BATC survey data. Various color-magnitude diagrams we can form with these data are presented in §4, where they are used in conjunction with theoretical models to derive estimates of the cluster age, metallicity, reddening and distance modulus. The binary fraction of stars on the MS, and the relationship of binaries to intrinsic scatter on the MS are discussed in §5. In §6 we discuss the spatial distribution of stars within M67 as a function of mass, as well as the overall shape of the cluster. The luminosity function (LF) and MF of M67 are discussed in §7 in the context of predictions from dynamical evolution of stars within a cluster that is over 100 relaxation times old. Our main conclusions regarding calibration of the BATC survey in general, and our scientific results on M67 in particular, are summarized in §8.

2. Observations & Data Reduction

2.1. Observations

BATC observations are done with the 0.6/0.9m f/3 Schmidt Telescope of the Beijing Astronomical Observatory (BAO), located at the Xinglong station of the BAO, altitude 900m, located about 150 km NE of Beijing. A full description of the BAO Schmidt, CCD and data-taking system, and definition of the BATC filter system are detailed elsewhere (Chen et al. 1996). We summarize those details in this section to the extent needed to

define our M67 observations.

The BAO Schmidt telescope is equipped with a Ford 2048×2048 CCD at its main focus, subtending 0.95 deg^2 of sky at $1.67''/\text{pixel}$. The passbands of the 15 filters in our system are shown in Figure 1, atop a typical southern Arizona night sky spectrum (the Xinglong night sky lacks the sodium-lamp emission lines). The central wavelengths and passband widths of the 15 filters are given in Table 1 along with identifying which filters are used for the present investigation. Note that all filters were designed to exclude most of the bright and variable night-sky emission lines, including the OH forest.

The primary calibration standard stars for the observations are chosen from flux standard list of Oke & Gunn (1983). Thus magnitudes in all 15 filters are on the Oke & Gunn’s AB magnitude system. Transformation from the AB magnitude system to UBVRI and other photometric systems can be found in Kent (1985), Edvardsson & Bell (1989) and Windhorst et al. (1991). We discuss this problem in detail using M67 observations in §3.2. Secondary flux standards will be developed in a number of ways during the BATC survey, of which selected stars in M67 from the present investigation form one subset. Our goal is to obtain five images of different integration times per filter per survey field, both in order to increase the dynamic range of our observations and to search for variable stars and active galaxies. We wish to reach the equivalence of $V = 21 \text{ mag}$ at a signal-to-noise (S/N) of 3 or better in most filters. The present M67 observations test the feasibility of this goal.

M67 was observed with the BAO Schmidt and nine BATC filters over six nights in Jan–Feb 1994. The log of observations is given in Table 2. We used the Number 1 2048×2048 Ford CCD, coated for UV response, with a nominal quantum efficiency of $\approx 20\%$ at 3200\AA , peaking around 44% at 6500\AA , and declining to 6% at 1μ (cf. Chen et al. 1996). Unfortunately, during the period of observation the UV efficiency of the coating declined somewhat while also increasing the non-uniformity of the UV flat-field. Owing to various

calibration constraints, we limited the number of BATC filters observed on a given night to be no more than five.

The No. 1 CCD had a readout noise of $8\text{ e}^-/\text{pixel}$ with gain adjusted to $3.2\text{ e}^-/\text{ADU}$ at the time of observation. When mounted at the f/3 main focus of the BAO Schmidt telescope, the CCD covers a field of view $58' \times 58'$, and has a linear scale of $1.67''/\text{pixel}$. The pixel scale somewhat undersamples the typical seeing conditions ($\sim 2\text{--}3''$) of the Xinglong site. Thus, one of the tasks of the M67 observations was to test the effect that this undersampling has on the eventual accuracy of the BATC survey.

The filters were divided into two groups for the M67 observations. Group A has four filters: 5795\AA , 6660\AA , 8020\AA and 9745\AA , while Group B has five filters: 3890\AA , 6075\AA , 7215\AA , 8480\AA and 9190\AA . Most of the observations were centered on M67 itself. For each filter group, one night was devoted to taking short exposure images offset from the central field by $10' - 15'$ in both RA and DEC direction and pointing the telescope to each of the four quadrants (I, II, III and IV) relative to the central M67 field (cf. Table 2). These “shift-field” pointings of the telescope permit a series of photometric and astrometric tests as summarized §3. A total area of 1.92 deg^2 , centered on M67, is observed in this way.

2.2. Flat-Fielding a Degree-Sized CCD Field

The large field of view of a CCD in a Schmidt Telescope, combined with the desire to observe many filters in a given night, presents a challenge for accurately flat-fielding the CCD. Over a one degree field (twice the angular size of the full Moon), neither the sky nor the twilight is uniform! Moreover, our use of intermediate-band filters that avoid bright night sky lines, combined with our desire to observe five filters per night, means that we cannot generally get sufficient sky photons for the calibration of the large-scale non-uniformities of

the CCD. However, to reach our goal of $\approx 1\%$ spectrophotometry, these large-scale non-uniformities must be calibrated to an accuracy of $<<1\%$.

After much experimentation (as described in Chen et al. 1996 and Yan et al. 1996), we found that a UV-transmitting diffuser plate, placed in front of the Schmidt entrance aperture, combined with a standard white-spot dome-flat system, is quite satisfactory. The scientific rationale for using such a diffuser plate is that, for a closed-tube structure such as a Schmidt telescope, an isotropic illumination at the entrance pupil is physically equivalent to a homogeneous source of illumination at infinity. The diffuser plate provides that isotropic illumination, even when the light source itself is not isotropic (tests were made even using the full Moon!).

Our tests, detailed in Chen et al. (1996), show that use of the diffuser plate yields large-scale and small-scale flat-field calibrations that are as good, if not better, than we can do using the night sky. Since the typical width of BATC filter is 300\AA , the color effect of flat-fielding due to the color difference of night sky and dome illumination is substantially reduced. As these flat-field calibrations are taken during the daytime, eight dome/diffuser flats can be taken with each filter. This means that, combined with the large full-well capacity of the CCD, our flat-fields are of signal-to-noise (S/N) >700 over the entire CCD.

In addition to the dome/diffuser flat fields, eight bias exposures are taken before and after each night. Dark exposures are not taken, as the dark current of the No. 1 CCD is very small (Chen et al.). All of the data for a given night: bias frames, dome/diffuser flat frames (serving the dual purpose of simultaneously calibrating pixel-to-pixel and large-scale gradient variations in the CCD), and program images are then fed into what is called the “Pipeline I” system, written by Zhaoji Jiang for the BATC survey.

Pipeline I programs subtract the clipped mean of 16 bias frames from each program frame, and divide it by the clipped mean of the eight flat-field exposures in the appropriate

filter. The astrometric plate solution is obtained by *a priori* knowing the approximate plate center position, and then using this information to register the brighter stars in each image with the Guide Star Catalog (GSC) coordinate system (Jenkner et al, 1990). Centroids of all the GSC stars in an image, typically >100 stars, are used to determine the plate solution. The astrometric error of GSC catalog is claimed to be $0.2'' - 0.8''$ per coordinate axis. The observed astrometric precision is estimated in §2.5 using the shift-field observations of M67. Pipeline I programs also calculate the altitude and azimuth of each image, as well as the relative direction and phase of the Moon. An example of the output of Pipeline I is shown in Figure 2, using one of the M67 centered observations with the 6075\AA filter.

2.3. Determination of the Point Spread Function

The point-spread-function (PSF) of the Schmidt-CCD-filter system was determined for each observation, using the six analytic PSF forms provided by DAOPHOT II (Stetson, 1987, 1992). After some experimentation, the “Penny” function was chosen, as it gave the smallest residual when fitting the data. The size of the PSF was permitted to vary linearly across the CCD, owing to an unavoidable slight tilt of the CCD surface relative to the focal plane. The FWHM of PSF typically changes $0.1''$ to $0.2''$ across the chip under the conditions when these observations were made.

Large numbers (~ 50) of relatively isolated and bright stars were chosen to permit study of cross-chip PSF variance. Once an approximate PSF width is obtained, all detected stars near candidate PSF stars are eliminated from the original frame and a more accurate PSF is then calculated. This process is iterated several times, first assuming no PSF variation over the CCD image. The linear spatial variation of the PSF is then determined after faint stellar neighbors of PSF stars are successfully eliminated.

After a satisfactory model of the PSF and its spatial variation over the CCD field is obtained, the ALLSTAR algorithm of DAOPHOT II is used to derive the stellar instrumental magnitudes from the image. An accuracy estimate is made, including contributions from readout noise, photon noise and non-perfect fitting errors.

An average FWHM value for each night of observation is given in Table 2, as measured from the PSF fitting results of filter 6075Å and 5795Å respectively. The limiting magnitudes for each filter given in Table 2 are estimated from the position where, in a histogram of star counts vs. apparent magnitude, star counts fall to 1/e the value of the peak. The limiting magnitude given here refers to the central region of M67 field (about $20' \times 20'$) which all six pointings covered. The limiting magnitude outside this central region, where only one short exposure was taken per position, is 1.5 mag shallower than in the center. A more accurate determination of limiting magnitude is complicated (Harris 1990) and unnecessary for the present paper.

2.4. Calibration to a Standard BATC System

Each filter group was observed during one photometric night: 17Jan94 for Group A, 2Feb94 for Group B. The Oke-Gunn primary flux standard stars HD 19445, HD 84937, BD+26° 2606 and BD+17° 4708 were observed during these two nights. Fluxes as observed through the BATC filters for the Oke-Gunn stars are predicted by convolving the SEDs of the Oke-Gunn stars with the measured BATC filter transmission functions. The night of 17Jan94 had high winds and poor seeing (cf. Table 2), resulting in somewhat poorer photometric accuracy for the Group A filters, compared to what is obtained for Group B. A summary of the photometric observations is given in Table 3.

BATC magnitudes are defined on the Oke-Gunn system as AB_v magnitudes with zero

point defined by :

$$m_i = -2.5\log f_{\nu_i} - 48.60. \quad (1)$$

Observations of the standard stars were done with a subset of the CCD for observing and data reduction efficiency. This was done after we had gained a large degree of confidence in our ability to accurately calibrate large-scale sensitivity variations in the CCD (cf. §2.2).

Standard stars were taken throughout both photometric nights at a range of air masses. In addition, we also used the fact that M67 itself has much UBVRI data to use a subset of the M67 stars as tertiary standards. Observations of the Oke-Gunn standards were used to determine the nightly mean extinction coefficients for each filter. Both the Oke-Gunn standards and the tertiary M67 standard stars were used to detect any change in the zero point of extinction over the night, as such variations are known to exist (cf. Colless et al. 1993):

$$m = a + m_0 + b \times \text{Air Mass} + f(\text{UT}). \quad (2)$$

No color term is used for atmospheric extinction, as the BATC filters are of intermediate (300Å) band-width and are designed to be fairly rectangular in shape. Verifiable UT variations of amplitude ± 0.015 mag were found during both photometric nights and were removed from the data.

The initial calibration of the Oke-Gunn stars showed a slight inconsistency among the calibration zero points, most likely owing to the known errors ($\sim 3\text{--}5\%$) in determining the filter transmission functions. Fortunately, all of the inconsistencies are at the ~ 0.01 mag level, and can be straightforwardly corrected (cf. Yan et al. 1996).

The mean values for the coefficients ‘a’ and ‘b’ in Equation 2, along with their 1σ errors

and the net 1σ residuals of fitting this equation to the data, are given in Table 3. As can be seen, the night of 17Jan94 (cf. above) has a zero point in the value of ‘b’ about 0.05 mag higher than for the night of 2Feb94. This likely indicates month-to-month variations in the extinction at the the relatively low altitude of the Xinglong site (900m). Note, however, that despite this change, the net fitting residual to the standard star observations are quite similar on the two nights. The formal error we obtain for the average of standard star residuals for nine BATC filters is 0.013 mag which, with reasonable estimates of external errors, indicates that we can define the standard BATC system to an accuracy of <0.02 mag.

2.5. The BATC M67 Spectrophotometry Catalog

The calibration of the M67 observations on the photometric nights was applied to the non-photometric nights in the following manner:

1. There are up to six exposures per filter. All stars found by DAOPHOT II in all exposures with photon noise less than 0.02 mag are used to determine the zero point difference between exposures. The individual exposure data for each star are then co-added by weight according to its S/N. This gives us one estimate of the S/N of the averaged stellar magnitudes. The photometric precision of each star is estimated by taking into account the noise contribution from every single exposure.

2. The observed magnitudes are then calibrated to BATC standard system by Equation 2.

3. BATC AB_v magnitudes and estimated magnitude errors are given for all filters of each star which is detected in at least 3 filters with magnitude errors of less than 0.3 mag. J2000 positions as calculated by the Pipeline I system (§2.2) are given, as well as the Sanders (1977) number for those stars in M67 so identified. The catalog that contains these data

for 6,558 stars centered on M67 are given in a file which can be electronically accessed as described at the end of this paper.

3. Accuracy of the Data

3.1. Photometric Precision

Sources of CCD photometric error include: photon statistics of star and sky; readout noise; random and systematic errors from bias subtraction and flat-fielding; image defects; possible non-linearity of the CCD; and from the PSF fitting and undersampling. The analysis program DAOPHOT II gives the theoretical prediction of the error based on the sky and stellar photon statistics it measures, and tries to estimate the extrapolation error from PSF fitting due to the undersampling of the data.

For those stars in common among the five shift-field exposures, we can estimate the net effect of these sources of error combined. In Figure 3 we explicitly calculate the dispersion in their DATPHOT II-measured magnitudes for all nine filters. We note again that these shift-field exposures are relatively short exposures in each filter and, as such, the errors we derive for faint stars will be lower limits to the precision we can attain with the BATC survey.

For each filter whose dispersion of measurement is shown in Figure 3, we overplot two lines: The solid line is the observed $1\text{-}\sigma$ error, while the dashed line is the theoretical prediction from DAOPHOT II. The fact that the dashed line is difficult to see in these diagrams indicates the high degree of consistency with which the BATC Pipeline I + DAOPHOT II programs have extracted stellar magnitudes from these images.

From this comparison, we conclude that the photometric precision for a single short BATC exposure is 0.02 mag for stars brighter than $m = 16$ in most filters, becoming larger

for faint stars. As the BATC survey will have at least five exposures per filter per field with these exposure times or longer, the photometric error for the BATC data is expected to be 0.01 mag for brighter stars. For example, for stars with $m_{7215} < 15.0$ mag, the observational error from five images is 0.01 mag, increasing to 0.15 mag for stars with $m_{7215} = 19.5$ mag (equivalent to an effective V mag of $19.5 - 20.0$) for a single exposure of 3 – 5 minutes.

Much of the scatter in the shift-field comparison comes from the undersampling of the PSF. When the image of the star only occupies a few pixels on the CCD, how that image projects on the pixel centers and edges becomes important. The difference of sub-pixel position is most serious when a star is near the limiting magnitude of observation. An astrometric precision of $\approx 0.3''$, which is what we would expect at the limiting magnitudes of the shift-field exposures is 0.2 pixels, so that the BATC magnitudes are sensitive to sub-pixel positioning issues. Undersampling of the star images affects the quality of BATC data in two ways: increasing the error of observation and complicating any calculation of the completeness function (cf. Stetson & Harris 1988).

The effect of undersampling on photometric errors can be tested using Group B filters, as stars in the 3890Å filter are slightly out-of-focus when stars in the other four filters are in focus (owing to a difference of 100μ of optical thickness in an f/3 beam). The FWHM of the PSF has a mean of $3.4''$ for the 3890Å shift-field exposures, which critically samples (at 2 pixels wide) the PSF. The observed $1-\sigma$ error is 0.015 mag compared to 0.013 mag as predicted by DAOPHOT II for bright stars with $m_{3890} < 13.0$. In contrast, the FWHM of the PSF's for the other four Group B filters averages as $2.4''$, or less than 1.5 pixels, and hence the star images in these filters are undersampled. In contrast, the observed $1-\sigma$ errors for the other four filters is 0.024 mag, compared to 0.027 mag as predicted by DAOPHOT II.

Hence, from this test we estimate the effect of undersampling on our photometric ac-

curacy to be close to 0.02 mag, as it adds quadratically to other random error components. This error accounts for most of the scatter observed in the photometric comparison for bright stars. The absolute zero point of the BATC system is calibrated here using the spectral energy distribution (SED) of HD19445 (Oke & Gunn, 1983), to an conservative accuracy of 0.02 mag.

Using the sub-pixel position, we separately examined how the limiting magnitude of stars depends on the placement of star images relative to pixel sides and corners. We find that when the star center falls directly on the pixel center, $m_{\text{lim}} = 19.2$ for a single 300s exposure in the 7215Å filter. In contrast, $m_{\text{lim}} = 18.7$ when the star center falls on a pixel corner, 0.5 mag fainter. In addition, while the histogram of star counts versus magnitude has a steep fall-off at the magnitude limit for centered stars, it has a much more gradual fall-off for stars on the corners. Fortunately, our ability to accurately determine star centroids relative to pixel placements permits us to better determine completeness limits, albeit in a complicated manner.

3.2. Comparison of the BATC Magnitude System with the UBVRI System

Of the available photometry of M67 stars, those of MMJ and of Gilliland et al.(1991) together cover the UBVRI system. In Figure 4 we present the relationships that can be formed between the BATC intermediate-band system and the UBVRI broad-band system. Stars in common between our data and those of these two data sources were matched by Sanders (1977) number, generally with $V < 15.5$. As such, random errors of observation are minimum for the comparison of these two data samples to the BATC photometry.

Equations 3–6 show the coefficients of the fits and their r.m.s. errors for the comparison of our filter colors with the B–V, V–I colors and V and I magnitudes of MMJ. Equations 7–10

show the fit coefficients and their errors for the comparison with the Gilliland et al.(1991) data (subscript G).

$$\begin{aligned} (B - V)_{\text{MMJ}} &= +0.137 \quad +0.474 \times (m_{3890} - m_{5795}) \quad -0.036 \times (m_{3890} - m_{5795})^2 \\ &\pm 0.020 \quad \pm 0.015 \quad \pm 0.022 \quad \pm 0.008 \end{aligned} \quad (3)$$

$$\begin{aligned} V_{\text{MMJ}} - m_{5795} &= -0.034 \quad +0.103 \times (m_{3890} - m_{5795}) \\ &\pm 0.029 \quad \pm 0.007 \quad \pm 0.007 \end{aligned} \quad (4)$$

$$\begin{aligned} (V - I)_{\text{MMJ}} &= +0.343 \quad +1.090 \times (m_{5795} - m_{8020}) \quad +0.196 \times (m_{5795} - m_{8020})^2 \\ &\pm 0.024 \quad \pm 0.015 \quad \pm 0.072 \quad \pm 0.083 \end{aligned} \quad (5)$$

$$\begin{aligned} I_{\text{MMJ}} - m_{7215} &= -0.362 \quad -0.381 \times (m_{6660} - m_{8020}) \\ &\pm 0.028 \quad \pm 0.004 \quad \pm 0.037 \end{aligned} \quad (6)$$

$$\begin{aligned} (B - V)_G &= +0.117 \quad +0.483 \times (m_{3890} - m_{5795}) \quad -0.029 \times (m_{3890} - m_{5795})^2 \\ &\pm 0.019 \quad \pm 0.015 \quad \pm 0.019 \quad \pm 0.005 \end{aligned} \quad (7)$$

$$\begin{aligned} V_G - m_{5795} &= +0.007 \quad +0.080 \times (m_{3890} - m_{5795}) \\ &\pm 0.017 \quad \pm 0.005 \quad \pm 0.004 \end{aligned} \quad (8)$$

$$\begin{aligned} (V - R)_G &= +0.002 \quad +1.299 \times (m_{5795} - m_{6660}) \\ &\pm 0.023 \quad \pm 0.012 \quad \pm 0.04 \end{aligned} \quad (9)$$

$$\begin{aligned} R_G - m_{6075} &= -0.042 \quad -0.561 \times (m_{6075} - m_{6660}) \\ &\pm 0.018 \quad \pm 0.007 \quad \pm 0.049 \end{aligned} \quad (10)$$

Comparison of the B–V fits to MMJ and Gilliland et al.(1991) shows evidence of a systematic difference of ≈ 0.02 mag between these two data sets, similar to what was found by MMJ. Comparison of the V magnitude transformation also shows evidence of systematic difference, of somewhat larger size (≈ 0.04 mag), in the sense that the Gilliland et al.(1991) V mag is fainter than that of MMJ at the same m_{5795} BATC mag. This is different than what MMJ found, and it is not clear what is the source(s) of difference. Despite the differences in transformation coefficients in B–V and V mag for Gilliland et al. and for MMJ, the errors in the fits are similar, ≈ 0.02 mag. Errors of similar size are seen in the V–I and I mag fits for MMJ, and the V–R and R mag fits for Gilliland et al.

We are wary of adopting any of these equations as defining the BATC filter relationship to broad-band colors, owing to these problems. As such, we present these relationships only as the external means of verifying our internal estimates of accuracy, rather than in terms of defining the slopes and zero points of these relationships. We leave that task for future work.

3.3. Astrometric Precision

J2000 coordinates for stars are obtained using the CCD coordinate frame established by the Pipeline I reduction package and the best-fit position of stars given by DAOPHOT II. The observed astrometric precision is calculated from the commonly observed stars in the five shift-field exposures, ensuring that the full CCD image is sampled. This comparison only tests for differences, random and systematic, between the BATC system and the GSC system. The astrometric accuracies for all nine BATC filters used in this paper were separately determined. Figure 5 shows the diagnostic plot that results for the 5759Å filter.

As is evident, the astrometric precision of the BATC survey relative to GSC system

is $\approx 0.15''$, or about $0.1''$ per coordinate axis, for magnitudes brighter than 17, becoming of lower precision for fainter stars. Thus, we have confidence that the BATC survey can predict relative positions of stars at least as accurately as the GSC itself, and are absolutely calibrated as well as the GSC system.

3.4. BATC Secondary Standard Stars in M67 field

Thirty stars are given by MMJ which appear to be suitable local photometric standards according to six criteria. Of these, all but one have observations in at least four images in each of the nine BATC filters used (one is too bright and is overexposed). As these stars do not appear to be variable, we also consider them suitable as secondary BATC standards. Their positions, nine color magnitudes, as well as their corresponding MMJ number and Sanders number (Sanders 1977) are listed in Table 4.

4. Color-Magnitude Diagrams

4.1. CMD Morphology

Cluster membership, as determined from the proper motion study of Girard et al. (1989), is known for the central region of M67 and for stars with $V < 16$. As our study is both deeper and of much larger angular extent from the Girard et al. study, contamination by field stars in our analysis will be handled statistically.

Figures 6–8 plot three representative color-magnitude diagrams (CMDs) that can be made from our data: $(m_{3890} - m_{6075})$ vs. m_{3890} (Figure 6) gives us the cleanest view of the CMD; $(m_{3890} - m_{9190})$ vs. m_{3890} (Figure 7) gives us the widest passband colors for these data that also goes to faint magnitudes; and $(m_{6075} - m_{7215})$ vs. m_{6075} (Figure 8) gives us

the deepest CMD. In each figure we present two graphs. The top graph is the whole data set, covering the field centered on M67 with a $40'$ radius (about the tidal radius of M67, see §6.1). The bottom graph contains only the data in the central $15'$ of the cluster, which correspond more closely to the data obtained by previous authors. Stars with known proper motion membership are given distinct plotting symbols, as explained in the figure caption. In Figure 9 we replot the $(m_{3890} - m_{6075})$ vs. m_{3890} CMD, but this time only using stars with membership probabilities of 80% or greater.

The morphology of the MS in these CMDs reveals much about the physical properties of this cluster.

a) A well-defined MS exists to $m_\lambda \approx 19 - 20$ mag in each CMD which covers the whole sample, but is less distinct at fainter magnitudes in the inner $15'$ sample. This difference, which pertains to mass segregation, is discussed at length below (§7).

b) The MS has a sharp blue edge and a soft red edge, with the redward scatter extending to ~ 0.75 mag brighter than the blue edge. Such a morphology of the MS indicates the presence of a populous binary star population in M67 (cf. Anthony-Twarog et al. 1990; MMJ). The binaries with nearly equal mass form a distinct sequence about 0.75 mag above the single star MS which is clearly seen in Figures 6 and 7.

c) The known blue straggler population in M67 is obvious, as well as an intrinsic dispersion in color and/or magnitude of stars near the main sequence turn-off.

d) Two gaps are seen along the MS, indicated by the arrows in the lower graphs in Figures 6–8. One gap is near the MS turn-off, the other gap is 1.4 magnitudes below the first gap.

e) These CMDs do not extend much brighter than $m_\lambda \approx 12$, as even in the shortest exposures (180s) stars brighter than $V = 10$ are saturated. As such, these data do not

measure the giant branch of this cluster brighter than the red clump stars at $m_{5795} \approx 10$.

f) The field stars exhibit a well-defined blue color limit in each CMD to about $m = 17$; fainter than this, one again finds more bluer stars. A similar blue cutoff to the brighter field stars is seen in broad-band CMDs (cf. Gilliland et al.; MMJ). We strongly suspect these faint bluer stars are either white dwarfs, some of which will belong to M67, and perhaps active extragalactic objects. We will explore these question further using spectroscopic data (Burstein et al. 1996).

All of the morphological features of the CMD of M67 we see here have been either pointed out by previous authors or are apparent on previously published CMDs (cf. Gilliland et al.; MMJ). There are two unique aspects about the present CMDs. First, the center wavelength of the 3890Å filter was a compromise between the stellar and extragalactic observers in the BATC survey. It covers the Ca II H,K break in the stellar spectrum, making the magnitude of that filter very sensitive to changes in effective temperature among A–G MS stars. As a result, m_{3890} changes rapidly with MS color, so that a CMD diagram such as Figure 6 or Figure 9 gives a rather vertical distribution of the MS, highlighting more clearly its morphology. This is the reason that the gaps in the MS more noticeable here than in previously published CMDs. Second, our observations determine the spectral energy distributions (SEDs) of bright stars in the M67 field to an accuracy of 0.02 mag. This permits us to investigate the stars in M67 both in terms of the morphology of the CMDs they form, and in terms of the morphology of their relative SEDs.

4.2. Isochrone Fitting

Uncertainties in the determination of the physical parameters of open clusters are both observational and theoretical in nature. On the observational side, uncertainties exist in

estimates of reddening (cf. Taylor 1982; Burstein, Faber & Gonzalez 1986), metallicity (Burstein et al. 1986), distance (MMJ), and scatter observed along the MS (cf. §5, above). On the theoretical side, authors using different models have obtained different results from the same data set. For example, Janes & Phelps (1994) show that the predicted age of M67 from “modern” CCD photometry ranges over nearly a factor of two, from 3.4 to 6 Gyr, more depending on whose model is used than which data set is fit.

For a new filter system such as the BATC filter set, we face the separate issue of defining these models in terms of our filter sensitivity functions. As we want to apply our observations equally to individual stars in our own Galaxy and to stellar populations in other galaxies, we opt for tying our filter system into the stellar evolutionary program of Worthey (1992; 1995), which also ties our observations to the Lick absorption-line-strength measurements of stars, globular clusters and galaxies (cf. Burstein et al. 1984; Faber et al. 1985; Gorgas et al. 1993; Worthey et al. 1994; Trager et al. 1996). At our request, Dr. G. Worthey has kindly calculated isochrones in our filter system for a range of stellar ages and metallicities, using the known BATC filter sensitivity curves and his stellar evolutionary models based primarily on the isochrones of Vandenberg (1985) (see Worthey 1994 for details) and the theoretical stellar SEDs of Kurucz (1992).

Figures 10 and 11 plot the Worthey-Vandenberg-Kurucz isochrones for a range of possible ages and metallicities for M67 over the CMDs formed by $(m_{3890} - m_{6075})$ vs. m_{3890} (Figure 10) and $(m_{6075} - m_{7215})$ vs. m_{6075} (Figure 11). We can narrow down the possible range of age and metallicity from these models in two ways.

First, one can see that the shape of the theoretical CMD near the MS turn-off does not match that observed in either Figure 10 or Figure 11 for isochrones older than 5 Gyr. Second, ages less than 3.5 Gyr require a more metal-poor stellar population ($[Fe/H] < -0.20$) than has been indicated by modern detailed investigations (cf. Burstein, Faber & Gonzalez

1986). This, then, leaves isochrones with ages between 3.5 and 5.0 Gyr and metallicities $[\text{Fe}/\text{H}] > -0.20$ as possible candidates.

Our best fit to the CMDs of M67 using these models derive an age of 4.0 ± 0.5 Gyr and a metallicity of $[\text{Fe}/\text{H}] = -0.10 \pm 0.05$. This fit is shown in Figures 10 and 11. The best-fit isochrone is given in Table 5. This fit was made to go through the observed main sequence in the $(m_{3890} - m_{6075})$ vs. m_{3890} diagram, as it is in this diagram that the MS is most accurately defined. Our tests (§5) strongly suggest that a large fraction of binaries exist in M67 and their presence contributes much of the scatter that is seen along the apparent single-star MS in CMD. As such, the best fit isochrone was made to fit *not* the the middle of the apparent single-star main sequence, but rather a parallel sequence 0.02 mag redder (equal to the $1\text{-}\sigma$ photometric error for bright stars) than the hard blue edge of the MS.

Previous workers (cf. MMJ) have commented on the fact that theoretical isochrones did not fit well the morphology of the MS turn-off as seen in broad-band CMDs for any reasonable choice of age and metallicity. In contrast, here we find that the 4.0 Gyr, $[\text{Fe}/\text{H}] = -0.10$ isochrone from the Worthy-VandenBerg-Kurucz model matches well the morphology of the main sequence turn-off in the $(m_{3890} - m_{6075})$ vs. m_{3890} diagram (Figure 10), but somewhat less well in the $(m_{6075} - m_{7215})$ vs. m_{6075} diagram (Figure 11).

As the accuracy of our intermediate band magnitudes is comparable to the accuracy of the broad band BVI data of MMJ (cf. §4,5), observational errors cannot be the sole source of this difference. We will explore another answer in §5 below, when we discuss the effect of binary stars on the M67 CMDs.

In principle the zero point in color and magnitude of the ischrone should provide the reddening and distance modulus of the cluster, especially when the isochrone fits the upper MS morphology as well as it does in Figure 10. The formal match of the 4.0 Gyr, $[\text{Fe}/\text{H}] = -0.10$ isochrone to the CMD in Figure 10 yields $(m - M)_0 = 9.47 \pm 0.05$ and $E(B-V) =$

0.052 ± 0.011 , using the fiducial reddening law of Scheffler (1982) to find $E(3890-6075) = 1.8 E(B-V)$. Yet, we note that with this fit to the main sequence, the zero point of the giant branch is too red, owing to the known problem of the Kurucz models not fitting the SEDs of cool stars well, especially at $\lambda < 4000\text{\AA}$ (cf. Worthey 1994; Clampitt & Burstein 1996).

This limitation of the Kurucz models also affects our predicted distance modulus and reddening using the present data. The CMDs formed by the redder BATC filters result in a rather small color spread of the upper main sequence (~ 0.1 mag; cf. Figure 11), making these CMDs much more sensitive to observational errors than colors formed using the 3890\AA filter. While the $m_{3890} - m_X$ colors that can be formed with this filter span over 1 mag in upper MS color, the zero points of Kurucz models in these colors are likely not accurate to better the equivalent of $\Delta E(B-V) = \pm 0.02$ mag (cf. the analysis of Clampitt & Burstein 1996). Instead, we use the limitations put on the possible reddening of M67 by Burstein et al. (1986), $E(B-V)$ between 0.015 and 0.052 mag, to place an upper limit on the possible zero point error in the 3890\AA filter to be 0.16 mag. In turn, this predicts an upper limit of the error in the predicted distance modulus of 0.16 mag.

4.3. Main Sequence Gaps

Existence of a gap in the distribution of stars near the MS turnoff region is a common feature of old open cluster like M67. This gap corresponds to the rapid change of the stellar structure of the stars as they approach hydrogen core exhaustion. The shape and size of the MS turnoff, and the relative position of the gap, is related to the effect of convection overshooting (cf. Demarque et al., 1994). In the isochrones, this gap is usually represented by a turn to the blue by the MS just below the actual turn-off luminosity. As can be seen in Figure 10, this is exactly where the Worthey-VandenBerg-Kurucz isochrone matches the observed gap in the stars, giving both added weight to the reliability of this fit and support

to this interpretation of the gap.

The existence of a second MS gap, 1.4 mag in the 3890Å filter below the first gap, is not *a priori* expected. Whereas the brighter gap is almost devoid of stars, the fainter gap is simply deficient of stars. We see this second gap in all CMDs made from the BATC filters, in all radial distances from the cluster center, as well as in the broad-band BVI CMDs of MMJ.

The question raised by this fainter gap is whether it is a statistical fluke in the initial mass function (IMF) of the cluster, or it is an indication of some physical process during stellar evolution that only affects a certain range in MS mass. Although similar gaps were seen in the broad-band CMDs published by McClure et al. (1981) for NGC 2420 and NGC 2506, of similar age and metallicity as M67, a more recent uvby investigation of NGC 2420 by Anthony-Twarog et al. (1990) shows little evidence of this gap.

Interestingly, this second gap appears at about a mass of $1 M_{\odot}$, where the calculations of Lattanzio (1984) point out that grain sedimentation in the forming star could increase the heavy metal content of the stellar core. The isochrone then calculated upon this assumption does have a second gap in the MS near stars of $1 M_{\odot}$.

This second gap (and the brighter gap) are easy to see in the CMDs of M67 owing to the large number of stars in this cluster (~ 1000 , see below). These gaps may not be as evident in CMDs of less populous clusters, or in CMDs with data of accuracy >0.05 mag in magnitude, nor will it be easily visible in CMDs in which the color coverage of M67 stars is relatively small (Fig 8). Future high-precision CCD photometry of other open clusters of similar age and mass as M67 should settle the question of whether this second gap is a statistical aberration or an indication of an important physical process in stellar evolution.

5. Percentage of Binaries among M67 Main Sequence Stars

The existence of a large binary population among the M67 MS stars is well-known (cf. Racine 1971; MMJ). It is evident in the CMDs of Figures 6–11 as the red “fuzziness” and blue hard edge of the MS, and as a scatter above the MS that is primarily within 0.75 magnitude. These facts have influenced other workers (cf. MMJ) to assume that M67 contains a bimodal distribution of binary star mass ratios, with some binaries formed of stars of near equal mass, and others combine stars of very unequal masses.

We use the precision of the present data set to reexamine the mass ratios and number of binaries in M67 from the following point of view: what would be the distribution of stars along the MS if all stars are in binaries, but the ratio of luminosity of secondary to primary is permitted to randomly vary from zero to unity?

We can look at the magnitude-color distribution of MS binaries in one of two ways: either in terms of a fixed primary mass, but varying secondary mass (termed iso-primary-mass binaries), or with same secondary/primary mass ratios (iso-mass-ratio binaries). The top graph in Figure 12 plots tracks of iso-primary-mass binaries as solid lines, while dashed lines are tracks of iso-mass-ratio binaries. The bottom graph in Figure 12 plots these predictions over the relevant subset of the actual M67 ($m_{3890} - m_{6075}$) vs. m_{3890} diagram. From inspection of the two parts of Figure 12 we can make four points:

a) All binaries with mass ratios (secondary mass/primary mass) from 0.0 to 0.5 are within 0.1 mag of the MS, even using a filter as blue as $\lambda_{\text{eff}} = 3890\text{\AA}$. To photometrically distinguish the low mass ratio binaries from single stars at the $> 3\text{-}\sigma$ level in CMDs requires measurements accurate to ≤ 0.03 mag, near the limit for stars in crowded fields. Fortunately, the field around M67 is not too crowded, and the proven accuracy of the BATC magnitudes is 0.02 mag for brighter stars.

b) Binary stars with mass ratios 0.9 to 1.0 aggregate near the equal-mass binary line. The fact that there are several stars with high membership probability significantly beyond the equal-mass binary line in Figure 12 suggests that some multiple star systems also exist in M67.

c) Binaries with mass ratios between 0.5 and 0.9 are spread out between the apparent single star MS and the apparent equal-mass binary MS. The above points show that an accurate CMD will have the appearance of having mostly equal mass binaries and single stars, rather than binaries with a continuity of mass ratios.

d) Near the MS turnoff, the luminosity contrast between the primary and secondary star increases, causing all binaries to have photometric properties more like single stars. This is especially true for red colors, where the color contrast between primary and secondary stars is smaller than for blue colors. Thus, at its upper end, the binary MS narrows, leading to a noticeable “fuzzy” appearance to the upper main sequence evident in Figures 6–9 and in other published CMDs of this cluster (cf. Gilliland et al. 1991; MMJ).

We further simulate the BATC filter observations using a “toy” open cluster with 1000 stars under the following assumptions: a) Main sequence stars follow the best-fitting isochrone of 4 Gyr, $[\text{Fe}/\text{H}] = -0.10$. b) The slope of MF is independent of mass for the MS, as we derive in §8 (below) for lower MS. c) A given star has a 50% chance of being a binary. d) The distribution of mass-ratios among the binary stars is random. e) The magnitudes of the stars are measured with a photometric precision of 0.02 mag in each passband. f) The primary stars have masses between $0.7 M_{\odot}$ and $1.3 M_{\odot}$. The simulated CMDs of $(m_{3890} - m_{6075})$ vs. m_{3890} and $(m_{6075} - m_{7215})$ vs. m_{6075} are shown in Figure 13. Comparisons of Figure 13 with Figures 6 and 8 show no qualitative difference in CMD morphology. The existence of an obvious photometric binary branch in the CMD of $(m_{3890} - m_{6075})$ vs. m_{3890} as well as the large scatter near the MS turnoff in both the observed and simulated CMDs,

suggest that M67 contains a large fraction of binaries.

We have calculated the star number distribution relative to the MS, taking the magnitude difference of each star from the fitted main sequence isochrone, independent of whether or not that star has a proper motion membership estimate. In Figure 14 we compare the observed distribution relative to the prediction of our toy model cluster which has 50% binaries based on the CMD of $(m_{3890} - m_{6075})$ vs. m_{3890} for the color range in $(m_{3890} - m_{6075})$ between 1.4 and 2.5 (colors are used, as binaries are most constant in color than in absolute magnitude). It is evident that model and real distributions are quite similar.

A noticeable feature of the real histogram distribution is that it is markedly asymmetric; more stars scatter to the red of the peak than to the blue. This asymmetry is also evident in the $(m_{3890} - m_{6075})$ vs. m_{3890} CMD (Figure 6) as a more sharply-defined blue edge to the main sequence than to the red edge (cf. discussion by MMJ). The model does very well in fitting this asymmetry, strongly implying that within what appears to be the single-star main sequence are also contained a substantial number of low mass-ratio binary stars.

If we do a straightforward accounting of obvious binaries, we find that 16% of the stars in M67 within $33.3'$ from the center are binaries with mass ratios 0.7 or higher according to their position on the CMD of $(m_{3890} - m_{6075})$ vs. m_{3890} . The background contribution is estimated and subtracted in the way described in §6.1. If we restrict our sample to the area observed by MMJ, we would derive an observed binary frequency of 22%, the same as derived by MMJ in the same mass-ratio interval.

The true binary fraction in this cluster depends critically on how we determine the contribution from low mass-ratio binaries. The asymmetric blue/red distribution of stars along the main sequence shows they exist and is consistent with the dynamical evidence discussed in §6.1. A more quantitative determination of their numbers is difficult both owing to errors in background determination and especially to the fact that it is difficult to

photometrically distinguish low mass-ratio binaries from single main sequence stars. MMJ tried to model the background and got a fraction of 38% for binaries of all mass-ratios.

As the agreement between model and data in Figure 14 shows, the most straightforward interpretation is that the binary mass-ratio distribution is random between 0 and 1. If so, then 50% of the stars in this cluster are binaries. However, by the same token, exactly how many low mass-ratio binaries are in this cluster is confused precisely because most of the low-mass ratio binaries have photometric properties so similar to those of single stars. As a result, while it is apparent there are many low mass-ratio binaries in M67, we also cannot rule out the binary fraction being somewhat less than 50%, or somewhat more.

The mass-ratio distribution of field binaries has been widely-studied. Trimble (1978) pointed out that the apparent distribution of binaries has two peaks in mass ratio, at 0.3 and 1.0. Previous investigators who estimated the binary frequency among cluster MS stars have used such a bimodal distribution for their estimates (cf. Anthony-Twarog et al. 1989; Mazzei & Pigatto 1988; MMJ). Later analyses of different samples of field binaries however, give very inconsistent results on the mass ratio distribution from bimodal to quite randomly distributed (cf. Trimble, 1990). In the case of M67, the binary distribution is more consistent with being randomly distributed than being double-peaked.

6. Spatial Distribution of Stars

6.1. Mass-dependent Spatial Distribution

It is well-known that M67 is sufficiently populous and dense to have a relaxation time much shorter than its age. For example, Francic (1989) gives the relaxation time of M67 to be 1.7×10^7 yr, while Mathieu & Latham (1986) calculate 10^8 yr. According to Binney & Tremaine (1989; pg. 526), the time it takes a star cluster to evaporate away is ~ 100

times the relaxation time, or in the case of M67, 2–10 Gyr (cf. calculations by Francic). As the estimated evaporation time is comparable to the age of the cluster, we would expect to see marked effects of mass diffusion, such as mass segregation among MS stars. With the present data set we can explore these issues explicitly.

Dynamical evolution of the cluster over time will progressively move the lower mass objects outward and the higher mass objects inward. The lowest mass objects in a cluster are, of course, the lower MS stars. The higher mass objects include the upper MS stars, subgiant stars and giant stars, as well as the binary stars. Dynamical evolution of the binary stars is likely to be separate from that of single stars, owing to the fact that energy can be exchanged between the binary orbits and the cluster orbits (cf. discussion by Binney & Tremaine, Chap. 8).

Until the present study, accurate photometric data of M67 stars were limited spatially, or large-scale studies had bright magnitude limits. Furthermore, estimation of field star contamination, important for understanding the low mass end of the MS of M67, was problematic. As a result, while MMJ were aware of the likelihood of mass segregation effects in their estimates of the cluster LF, they could not explicitly measure it.

The present observations are well-suited in terms of field size and depth of study. Field star contamination can be estimated with the present data set given a reasonable value for the tidal radius of M67. According to Von Hoerner (1957), the tidal field of the Galaxy produces a tidal radius R_t defined as:

$$R_t = R_G \times \left(\frac{M_c}{2M_G}\right)^{1/3}, \quad (11)$$

where R_G is distance to the galactic center, M_G is the total mass of the Galaxy within R_G . Outside of R_t , the tidal field of the Galaxy is predicted to strip stars away from M67, so

beyond this radius can be considered the “field.” Francic (1989) gives $R_t = 42'$ for M67 (using the distance modulus of Francic). By coincidence, the largest radius from the center of M67 at which our data can reasonably sample stars in a full annulus is $42.5'$. Hence, we choose an annulus of $37.5'$ to $42.5'$ from the center of M67 to sample the “field.” A star outside of the tidal radius is also not necessarily being evaporated from the cluster immediately. So by choosing the annulus in this way, we are slightly underestimating the number of the very outer-most M67 stars.

Figure 15 shows the apparent magnitude function of the field stars. The differential star counts $A(m)$ between m_{5795} of 14 and 18 is roughly proportional to $10^{-0.2m}$. This is consistent with the prediction based on galactic models (Bahcall & Soneira, 1980, 1984), indicating that the contribution from M67 members in this annulus is negligible.

Figure 16 plots the cumulative radial distributions for seven subsets of the M67 stars, with their estimated field star contamination removed: subgiants+giants, three absolute magnitude ranges of MS stars, blue stragglers, and two absolute magnitude ranges of obvious photometric binary stars. Following Mathieu & Latham (1986), we give a lower limit of $2M_\odot$ to the mass of blue stragglers and assume they should be compared to the binary distribution, not the single star distribution. Stars are classified based on their positions in the $(m_{3890} - m_{6075})$ vs. m_{3890} CMD and the best-fit isochrones given in §4.2. The binaries are those with mass ratios estimated according by the binary model of §5 as being 0.7 or larger.

Mathieu & Latham (1986), Francic (1989) and MMJ all give evidence of mass segregation in M67. The mass and half-mass radius for each stellar subset of the present data are given in Table 6, and span an average mass range from $0.7 M_\odot$ to at least $2 M_\odot$. Lower limits are given for the masses of MS stars, subgiants and giants, owing to the existence of binaries with small mass-ratios.

Interestingly, if we separate our sample into mostly single stars plus low-mass-ratio binaries, versus obvious photometric binary stars and blue stragglers, a significant trend is found in terms of mass segregation: Among the higher mass objects, blue stragglers are the most concentrated and thus implied to be most massive; obvious binaries of lower mass are the least concentrated, but are still more concentrated than any of the MS “single” stars. Among the “single” stars, there is some evidence that degree of concentration increases with increasing mass, albeit with somewhat large errors.

All of the nominal “single” MS stars have half-mass radii significantly smaller than all of the binary stars. This pattern is consistent with the suggestion that the more massive binary stars dynamically behave almost as if in a different cluster than the single stars (cf. Binney & Tremaine, 1989; Chapter 8). Both numbers and high masses are consistent with the idea that blue stragglers evolve from near equal-mass-ratio binary systems (cf. Mathieu & Latham, 1986).

We also investigated if we could detect mass segregation among the low mass-ratio binary stars whose photometric properties place them near the single-star MS. Using the fitted isochrone in the $(m_{3890} - m_{6075})$ vs. m_{3890} CMD and in the same magnitude level as the other tests on MS stars, we separated the stars into “blue” side (-0.05 to 0.02 mag from the isochrone) and “red” side (0.02 to 0.09 mag from the isochrone) of the MS (MS ‘b’ and MS ‘r’, respectively in Table 6), and then calculated their spatial distribution. While we do see a difference in the expected sense, the difference is small relative to the observational error.

The data in Table 6 and plotted in Figure 16 provide ample evidence that dynamical evolution has substantially modified the distribution of stars in M67. Indeed, M67 has a halo made mostly of faint low mass stars and a core made primarily of high mass binaries plus giant, subgiant and upper main sequence stars. It is apparent that, in M67, we are looking

at a cluster in the process of evaporation. Below, we suggest one way the evaporation rate might be calculated in the observed mass range.

6.2. The Shape of M67

Our data can give a hint of the two-dimensional shape of M67. In Figure 17 we plot the CMDs obtained at nine different positions around M67. The inner CMD comes from a radius of $< 5'$ of the cluster center, while the outer 8 CMDs are taken in pie-shaped cuts of 45° angle, between radii of $5'$ and $16.67'$. These cuts are positioned in Figure 17 such that the north cut is up and the east cut is to the left.

A well-defined M67 MS is evident from the NE to SW direction, but is ill-defined in NW and SE directions. To better see this, we counted the number of stars along main sequence locus vs. all other stars as background between $14 < m_{3890} < 19$ in the eight cuts around the center. We found 35.5 ± 0.6 MS stars per area in NE, S, SW, W panels and 22.5 ± 1.7 MS stars per area in N, NW, SE, and E panels. In contrast, the number of background stars per region is 21.5 ± 3.3 . Thus we see a $> 3\sigma$ difference in MS star counts between the NE-SW direction and the NW-SE direction.

This indicates that M67 is elongated at a position angle of $30^\circ \pm 45^\circ$, or $15^\circ \pm 45^\circ$ relative to Galactic plane. It is not too surprising that a Galactic cluster as old as M67 has an elliptical shape, given the tidal stresses to which has been subjected over its lifetime. Terlevich (1987) used N-body simulations to predict that the flattening of evolved open clusters will produce major axes parallel to the Galactic plane. Our result here is consistent with her simulation.

7. Luminosity Function and Mass Function

7.1. Luminosity Function

The previously-derived LF for M67 show a maximum near the MS turnoff, and a decline with fainter main sequence magnitudes (van den Bergh & Sher, 1960, Francic 1989; MMJ). MMJ pointed out that this decline could be an artifact of mass segregation and mass loss. Certainly the analysis of the previous section supports this view, which we explicitly examine here.

To accurately derive the faint end of the LF for M67, we need to understand our selection criteria, which means determining the limiting magnitude of our data as a function of distance from the cluster center. As discussed before (§3), our data are comprised of many exposures obtained under different observing conditions and subject to different magnitude limits, owing to different exposure times and effects of undersampling. In particular, the longest exposures were taken of the cluster center, over a nearly one-degree field of view, while the extension of our data to twice this angular extent was done with shorter exposures.

Thus, we decided to limit the LF analysis to the passband that goes the deepest across the whole region sample — 7215\AA . To avoid undersampling problems, we limit our analysis to stars which have $m_{7215} < 18.0$ mag. The correction for field star contamination is done in the same way as in the spatial distribution analysis.

Figure 18 shows the LF for M67 as found in three volumes: a) from 0 to $5'$ (“cluster core”); b) 0 to $16.67'$ (“intermediate cluster”); and c) 0 to $33.33'$ (“whole cluster”). We find that the 7215\AA LF for the “cluster core” peaks at $m_{7215} = 12.5$ mag; one magnitude below the MS turn-off. This is consistent with what Francic (1989) and MMJ found. Contributions from binaries are included when computing LF.

In contrast, the LF for the “intermediate cluster” rises quickly at the MS turnoff, and then remains fairly flat within errors to the magnitude limit. The LF for the “whole cluster”

reinforces the trend seen in the intermediate cluster, showing a slight trend of increasing star numbers down to the magnitude limit. There is also a marked deficit of stars at $m_{7215} \approx 16.5$, corresponding to $V \approx 16$, which only appears when the outer annuli of M67 are included.

Hence, previously voiced suspicions (cf. MMJ) about the effect of mass segregation on the observed LF of M67 are confirmed. As is even clear from the CMDs in Figures 6–9, low mass MS stars are predominantly found in the outer parts of M67, while the higher mass main sequence stars are found in the inner part.

7.2. Observed Mass Function and Effects of Dynamical Evolution

The MF for stars is commonly written in the form of a Salpeter (1955) power law: $dN(M) \propto CM^\eta dM$. Scalo (1986) finds $\eta = -2.00 \pm 0.18$ for field stars. Francic (1989) finds a similar slope for six young clusters ($\eta = -1.97 \pm 0.17$). In contrast, Francic derived $\eta = +3.63$ for NGC 752, another old open cluster and $+2.49$ for M67 in the V passband. Prata (1971) theoretically studied the evolution of the MF of M67, and concluded that IMF of M67 is likely to be deficient in low-mass stars. With our current sample we can test this idea explicitly.

We use the best-fitted Vandenberg (1985) isochrone (i.e., 4 Gyr, $[\text{Fe}/\text{H}] = -0.10$) to establish the relationship between absolute magnitude and mass to derive the LF for M67. Field star contamination is corrected as before. We fit the data with a Salpeter power law within mass range of $0.5 M_\odot$ to $1.2 M_\odot$. The results of the fitting are given in Table 7 as a function of increasing volume sampled in M67. As is evident, we obtain a MF of $+1.12$ for the cluster core, but -0.51 for the whole cluster.

Figure 19 shows the MF for the whole M67 cluster (to a radius of $33.33'$), to a limiting mass of $0.5 M_\odot$ up to the MS turnoff. A slope of $\eta = -2.0$ is shown superimposed on the

massive end of the MS. A formal MF for stars with masses between 1.2 and 0.8 M_{\odot} is fitted by a power law with $\eta = -1.93 \pm 0.66$. It is evident that the slope of the MF changes from having $\eta \sim -2.0$ for the mass range 1.2 – 0.8 M_{\odot} to $\eta \sim 0$ (i.e., independent of mass) for lower mass stars (0.8 – 0.5 M_{\odot}). Any residual contamination by M67 member stars in our star background is unlikely to significantly change the lower mass MF slope. Similarly, from the excellent fit to the Bacall and Soneira model, especially at the fainter end (Figure 15), we conclude the change of slope in the MF at 0.8 M_{\odot} is real.

The fact that we observe the effects of dynamical evolution among the stars that currently define M67 as a cluster strongly suggests that low mass stars have selectively evaporated from the cluster over time. This is consistent with theoretical estimates, which place the evaporation time scale for M67 comparable to its age (cf. Prata 1971; Francic 1989; §6.1 above). One kind of quantitative estimate of the number of lost stars (at least down to a mass of 0.5 M_{\odot}), can be made if we assume that M67 started out with a Scalo IMF slope of $\eta = -2.0$. We then take this best fit $\eta = -2.0$ slope for masses 1.2–0.8 M_{\odot} , and extrapolate this to the lower MS masses. From this we predict ~ 450 stars in the mass range 0.8 to 0.5 M_{\odot} have evaporated from this cluster over its 4 Gyr age, or at an average rate of one star per 10 million years. Such a mass loss rate, while not proven by this calculation, is plausible. From this comparison we conclude that it is equally plausible that the IMF of M67 followed a Salpeter power law with the canonical field star value of $\eta = -2.0$.

Our observed mass estimate for M67 is larger than previous estimates owing to the fact that we have sampled a larger volume of the cluster to fainter limits than previous surveys (cf. Mathieu 1985; Francic 1989; MMJ). In Table 7 we compute the observed mass of M67 within an increasing radial distance from the cluster center, giving both the single star estimate and that we would estimate from both binary and single stars.

8. Conclusions

These M67 observations are but the first of many such observations of galactic clusters and galactic fields pertaining to studies of Galactic structure, which we will obtain with the BATC survey. By using this open cluster as a calibration source, we are able to show the accuracy of the data we can obtain with the 0.6m/0.9m BAO Schmidt telescope at its Xinglong, China site. It is evident we can obtain spectrophotometry from the ultraviolet to $\sim 1\mu$ down to an intrinsic accuracy of better than 0.02 mag for all objects in the nearly 1 deg² field of the CCD, using Oke–Gunn primary standard stars (Oke & Gunn 1983). Similarly, we can define the positions of these objects to an accuracy of 0.15" for bright stars, using the Guide Star Catalog (Jenkner et al. 1990). To reach these accuracies, and to be able to observe through as many as five filters in a given night, we have used a diffuser plate in combination with our dome flat fields to obtain flat fields at least as accurate as we could obtain using sky observations.

Our observations of M67 span an area $1.92^\circ \times 1.92^\circ$ centered on the cluster in nine BATC intermediate-band filters. The color magnitude diagrams formed from these data show morphologies consistent with previous CMDs of M67, as well as defining better than most the gap in the MS near the MS turn-off. Isochrones of a range of appropriate stellar populations has kindly been made available by Dr. G. Worthey. These models, which convolve our filter sensitivity curves with his theoretical spectral energy distributions (based on the theoretical stellar evolutionary tracks of VandenBerg (1985) and the synthetic stellar spectra of Kurucz (1992)), have been fitted to our data.

We show that the combined Worthey–VandenBerg–Kurucz model fits the $(m_{3890} - m_{6075})$ vs. m_{3890} CMD very well for an age of 4 Gyr and $[\text{Fe}/\text{H}] = -0.10$, yielding a reddening of $E(B-V)$ between 0.015 and 0.052 mag and a distance modulus $(m - M)_0 = 9.47 \pm 0.16$ mag. The uncertainties in the derived distance modulus and cluster reddening are dominated by

uncertainties in the predicted Kurucz fluxes below 4000\AA . As such, we use the range of known reddenings for M67 to place limits on what are these uncertainties.

It is well known that M67 has a parallel binary main sequence. We find that 16% of stars in M67 are binaries with mass-ratio larger than 0.7, in agreement with previous studies. In a departure from previous work, here we model the binary star population of M67 in terms of a random distribution of secondary/primary mass-ratios from 0.0 to 1.0. We find that even if the mass-ratio distribution of binaries in the cluster is random, there will still be an apparent offset, parallel MS in the CMD. Although we cannot accurately determine the fraction of low mass-ratio binaries in the cluster, our data are consistent with 50% of the observed stars in M67 being binaries.

As our survey of M67 combines deep images, accurate photometry and a wider field coverage than previous surveys, we are able to explore dynamical evolutionary issues pertaining to this old galactic cluster. We find much evidence of substantial dynamical evolution of M67. The spatial distribution of stars is clearly dependent on their masses. Blue stragglers are the most centrally-condensed among the stars, consistent with previous observations (cf. Mathieu & Latham 1986). The assumption that blue stragglers are binary stars of nearly equal mass ratio is consistent with the steady decrease in central concentration observed from blue stragglers to lower mass binaries with secondary/primary ratios > 0.7 . A similar trend is seen among the “single” stars — giant star to lower mass main sequence stars — where the word single is in quotes owing to a likely contamination by low-mass-ratio binary stars. Overall, the binary stars as a group are more centrally condensed within M67 than are the “single” stars. With these data we can also investigate the two-dimensional shape of M67, which we find to be elongated along an angle of $15^\circ \pm 45^\circ$ relative to the Galactic plane.

Similarly, we find that the luminosity function (LF) of M67 is dependent on the volume

samples. If we observe only the inner core of the cluster, we find results similar to those previously obtained, in which there are more stars on the upper MS than on the lower MS. However, if we include the cluster stars out to a radius of $33.33'$ (within the tidal radius estimated by Francic (1989)), we find a LF that rises from the MS turnoff and then flattens out at fainter absolute magnitudes.

We use the isochrone fit of the Worthey-VandenBerg-Kurucz model, combined with our model of binary star distribution, to derive a mass function (MF) for M67 at its present age. Using the Salpeter (1955) definition of a MF power law, we find the slope η (as in M^η) to be near the canonical field star value of -2.0 for MS stars with masses between 1.2 and $0.8 M_\odot$, but which levels off for lower mass stars to the limit of our observations (at $0.5 M_\odot$). If we attribute this leveling off as due to evaporation of stars through dynamical evolution of this old cluster, we estimate that M67 has lost one star of mass between $0.8 M_\odot$ and $0.5 M_\odot$ every $\sim 10^7$ years.

Hence, with these data we have been able to observe both direct and implied evidence of substantial dynamical evolution of M67, consistent with theoretical expectations. We note that our data show an old open cluster whose most likely binary fraction and IMF are remarkably consistent with that of the field.

Files in standard ADC format, giving the full BATC data for all 6558 stars can be accessed either via anonymous ftp from [samuri.la.asu.edu](ftp://samuri.la.asu.edu) (IP 129.219.144.156), in the sub-directory `pub/m67`, or from the Astronomical Data Center (ADC).

We thank Guy Worthey for providing the theoretical isochrones under BATC colors, David Marcus for his help with the BATC filter design, Sam Pascarelle for the calibrated MMT night sky spectrum, and Jeremy Goodman for helpful discussion. We also thank the referee for valuable comments and suggestions. This research is supported in part by

an International U.S. NSF Grant INT-93-01805, by the National Science Foundation of China, by Arizona State University, the University of Arizona and Western Connecticut State University and by the National Science Council of Taiwan under the grant NSC84-2112-M-008-024.

REFERENCES

- Anthony-Twarog, B.J., Twarog, B.A., & Shodhan, S., 1989, AJ, 98, 1634
- Anthony-Twarog, B.J., Twarog, B.A., Kaluzny, J., & Shara, M.M., 1990, AJ, 99, 1504
- Bahcall, J.N., & Soneira, R.M., 1980, ApJS, 44, 73
- Bahcall, J.N., & Soneira, R.M., 1984, ApJS, 64, 53
- Bergbusch, P.A., VandenBerg, D.A., Infante, L, 1991, AJ 101, 2102
- Binney, J. & Tremaine, S. 1989, *Galactic Dynamics*, Princeton University Press: Princeton.
- Burstein, D., Faber, S.M., Gaskell, C.M & Krumm, N. 1984, ApJ 287, 586
- Burstein, D., Faber, S.M. & Gonzalez, J.J. 1986, AJ 91, 1130
- Burstein, D., et al., 1996, in preparation
- Chevalier, C., & Ilovaisky, S.A., 1991, A&AS 90, 225
- Chen, J.S., et al., 1996, in preparation
- Clampitt, L. & Burstein, D. 1996, in preparation
- Colless, M., Saglia, R. P., Baggle, G., Burstein, D., McMahan, R. K., Wegner, G., Davies, R. L. & Bertschinger, E. 1993, MNRAS 262, 475
- Demarque, P., Sarajedini, A., & Guo, X.-J., 1994, ApJ 426, 165
- Edvardsson, B., & Bell, R.A., 1989, MNRAS, 238, 1121
- Faber, S.M., Friel, E.D., Burstein, D. & Gaskell, C.M., 1985, ApJS 57, 711
- Francic, S.P., 1989, AJ 98, 888

Gilliland, R.L., et al., 1991, AJ 101, 541

Girard, T.M., et al., 1989, AJ 98, 227

Gorgas, J., Faber, S.M., Burstein, D., Gonzalez, J.J., Courteau, S. & Prosser, C. 1993, ApJS
86, 153

Harris, W.E., 1990, PASP 102, 949

Janes, K.A., & Phelps, R.L., 1994, AJ, 108, 1773

Janes, K.A., & Smith, G.H., 1984, AJ 89, 487

Jenkner H., et al., 1990, AJ, 99, 2082

Johnson, H.L., & Sandage, A.R., 1955, ApJ 121, 616

Kent, S.S., 1985, PASP, 97, 165

Kurucz, W. 1992, in IAU Sym. 149, The Stellar Population of Galaxies, ed. B. Barbuy & A.
Renzini (Dordrecht, Kluwer), 225

Lattanzio, J.C., 1984, MNRAS 207, 309

Mathieu, R.D., & Latham, D.W., 1986, AJ 92, 1364

Mazzei, P., & Pigatto, L., 1988, A&A 193, 148

McClure, R.D., Twarog, B.A., & Forrester, W.T., 1981, ApJ 243, 841

Montgomery, K.A., Marschall, L.A., & Janes, K.A., 1993, AJ 106, 181 (MMJ)

Nissen, P.E., Twarog, B.A., & Crawford, D.L., 1987, AJ 93, 634

Oke, J.B., & Gunn, J.E., 1983, ApJ 266, 713

Prata, S., 1971, AJ, 76, 1071

Racine, R., 1971, ApJ 168, 393

Salpeter, E.E. 1955, ApJ 121, 161

Sanders, W.L., 1977, A&AS 27, 89

Scalo, J.M., 1986, Fund. Cosmic Phys 11, 1

Scheffler, H., 1982, in Landolt-Börnsterin Nurmerical Data and Functional Relationships in
Science and Technology, Group VI, Vol. 2

Schild, R.E., 1983, PASP 95, 1021

Stetson, P.B., 1987, PASP 99, 191

Stetson, P.B., 1992, PASP 25, 297

Stetson, P.B., & Harris, W.E., 1988, AJ 96, 909

Taylor, B.J., 1982, Vistas Astron 26, 253

Terlevich, E., 1987, MNRAS, 224,193

Thuan, T.X., & Gunn, J.E., 1976, PASP, 88, 543

Trager, S., Faber, S.M., Gonzalez, J.J., Worthey, G., & Burstein, D. 1996, in preparation

Trimble, V., 1978, Observatory 98, 163

Trimble, V., 1990, MNRAS, 242, 79

VandenBerg, D.A., 1985, ApJS 58, 711

van den Bergh, S., & Sher, D., 1960, Publ. D. Dunlap Obs., 2, 203

von Hoerner, S., 1957, ApJ 128, 451

Windhorst, R.A., et al., 1991, ApJ, 380, 361

Worthey, G., 1992, Ph.D. Thesis, U.C. Santa Cruz, CA

Worthey, G., 1994, ApJS, 95, 107

Worthey, G. 1995, private communication

Worthey, G., Faber, S.M, Gonzalez, J. & Burstein, D. 1994, ApJS 94, 687

Yan, H.J, et al, 1996, in preparation

Figure Captions

Figure 1. Transmission curves of the BATC filters superimposed on a typical sky spectrum. The Number 10 filter (7215Å) was used at the time when the M67 data were taken. Later, this passband was divided among filters 10a (7050Å) and 10b filter (7490Å). Note that most of the important sky lines are avoided by the BATC filter bandpasses.

Figure 2. The central $58' \times 58'$ field of view of the BATC CCD, centered on M67. North is up, East is left. The scale of the image is given by the arrow at the lower-right corner. Numbers at the bottom, left, top and right sides, respectively, are R.A. and Dec. (2000.0) and the angles of azimuth and altitude of the field at the time of observation.

Figure 3. Photometric precision in 9 filters computed from five shift-field exposures. Delta mag is the magnitude difference between a single observation and the average of five observations. The thick solid line is the average of observed scatter while the thick dashed line is the average of predictions given by DAOPHOT II. Note the DAOPHOT II predictions somewhat overestimate the 1σ errors actually observed.

Figure 4. The relationship between BATC magnitudes and UBVRI magnitudes. BATC magnitudes are compared with BVI observation of MMJ (1993) (left hand side of figure) and the BVR observations of Gilliland et al. (1991) (right hand side of figure). The scatter in these correlations is typically 0.02 mag.

Figure 5. The internal astrometric precision of the BATC data, computed from five shift-field exposures. The solid line is the 1σ scatter of the observations.

Figure 6. The $(m_{3890} - m_{6075})$ vs. m_{3890} color magnitude diagram (CMD) for M67. The upper graph is for the whole field observed around M67; the lower graph is only for the stars within $15'$ of the cluster center. Stars with different membership probabilities (Girard et al.

1989) are marked with different symbols: $> 90\%$: plus signs; $80\% \leq 90\%$, open circles; $50\% \leq 80\%$: stars; $< 50\%$: crosses. Stars with no measured membership probabilities are plotted as points. This CMD gives us the cleanest view of the main sequence of M67.

Figure 7. The $(m_{3890} - m_{9190})$ vs. m_{3890} CMD. Symbols are the same as in Figure 6. This CMD gives us the widest passband colors that also go to the faintest magnitudes.

Figure 8. The $(m_{6075} - m_{7215})$ vs. m_{6075} CMD. Symbols are the same as in Figure 6. This CMD goes the faintest of all the BATC filter observations.

Figure 9. The $(m_{3890} - m_{6075})$ vs. m_{3890} CMD, now showing only those stars with membership probability $> 80\%$.

Figure 10. Worthey-VandenBerg-Kurucz isochrone models fit to the observed $(m_{3890} - m_{6075})$ vs. m_{3890} CMD. $(m - M)_0 = 9.47$ and $E(B-V) = 0.05$ are assumed; see text for details. The values of age and $[Fe/H]$ of each isochrone are shown in the graphs. Data for stars with known membership probabilities $\geq 80\%$ are plotted as open circles; all other stars are plotted as dots.

Figure 11. Worthey-VandenBerg-Kurucz isochrone models fit to the observed $(m_{6075} - m_{7215})$ vs. m_{6075} CMD. Same models, distance modulus and $[Fe/H]$ as for Figure 10.

Figure 12. (a) Tracks of iso-primary-mass binaries and iso-mass-ratio binaries in the $(m_{3890} - m_{6075})$ vs. m_{3890} CMD. Iso-primary-mass tracks are plotted as solid lines in steps 0.02 in the primary mass; iso-mass-ratio tracks as dotted lines in steps of 0.05 in secondary/primary mass ratio. (b) Same tracks plotted over the observed M67 $(m_{3890} - m_{6075})$ vs. m_{3890} CMD; data for stars with membership probabilities $> 80\%$ are plotted as open circles.

Figure 13. The results of our “toy” model of a stellar population of age and metallicity

similar to M67 that has 50% of its stars being binaries with a random distribution of binary mass-ratios. (a) The predicted distribution of stars in the $(m_{3890} - m_{6075})$ vs. m_{3890} CMD. (b) The predicted distribution of stars in the $(m_{6075} - m_{7215})$ vs. m_{6075} CMD.

Figure 14. The distribution of stars relative to single star MS for real data (solid) compared to that obtained from the “toy” model (dashed). Only stars with colors $(m_{3890} - m_{6075})$ between 1.4 and 2.5 are used for this histogram, both model and real data. The fiducial single star MS is defined as the 4 Gyr, $[\text{Fe}/\text{H}] = -0.10$ Worthey-VandenBerg-Kurucz model from Figure 10. The apparent bimodal distribution of stars, with one peak at the single star isochrone and the other 0.7 mag brighter, is evident. However, the asymmetric shape of the “single” star peak, which scatters preferentially towards brighter mags and redder colors, implies the existence of large numbers of low-mass-ratio binary systems in M67 masquerading as apparent single stars. Note that the real star distribution includes all stars in this magnitude interval, known member or not.

Figure 15. The apparent magnitude distribution of field stars, as obtained within an annulus of $37.5'$ to $42.5'$ in radius from the M67 cluster center. The dashed line is the predicted magnitude distribution of the Bahcall & Soneira (1980) model.

Figure 16. The observed cumulative radial distributions for seven kinds of M67 stars: subgiants+giants (light solid line); three absolute magnitude ranges of MS stars — $13.8 < m_{3890} \leq 14.5$ (heavy solid line), $14.5 < m_{3890} \leq 15.6$ (long dashed line) and $15.6 < m_{3890} \leq 18.5$ (dark dot-dashed line); blue stragglers (light dotted line), and two absolute magnitude ranges of photometric binary stars — $14.5 < m_{3890} \leq 15.6$ (light dot-dashed line) and $15.6 < m_{3890} \leq 18.5$ (dash-dot-dot-dotted line).

Figure 17. The $(m_{3890} - m_{6075})$ vs. m_{3890} CMD as observed in nine different positions centered around M67. The M67 MS stands out clearly along the upper-left (NE) to lower-

right (SW) diagonal, yielding an angle of 15° relative to galactic plane) and an elliptical shape for this cluster.

Figure 18. The observed 7215\AA luminosity function of M67 separated into three volumes of increasing size: (a) to a radius of $5'$; (b) to a radius of $16.67'$ and (c) to a radius of $33.33'$. See text for a full discussion of this figure.

Figure 19. The observed mass function for the whole cluster, as derived from the luminosity function of Figure 18c, combined with the isochrone fit of the Worthey-VandenBerg-Kurucz model. The lower mass limit is $0.5 M_\odot$ and the dashed line is a $\eta = -2.0$ Salpeter law fit to the stars with masses 1.2 to $0.8 M_\odot$.

Table 1. The BATC Intermediate-Band Filter Set

Filter No.	CW(Å)	FWHM(Å)	Observed ?
1	3360	360	No
2	3890	340	Yes
3	4210	320	No
4	4550	340	No
5	4925	390	No
6	5270	340	No
7	5795	310	Yes
8	6075	310	Yes
9	6660	480	Yes
10a	7050	300	No
10	7215	550	Yes
10b	7490	330	No
11	8020	260	Yes
12	8480	180	Yes
13	9190	260	Yes
14	9745	270	Yes

Table 2 : Observation Log, 7Jan94 – 2Feb94

Date	3890Å	5795Å	6075Å	6660Å	7215Å	8020Å	8480Å	9190Å	9745Å	FWHM
(yymmdd)	(sec)	(sec)	(sec)	(sec)	(sec)	(sec)	(sec)	(sec)	(sec)	(arcsec)
940107		180		180		180			360	2.1
940109		1200		1200		1200			3600	3.2
940117 (I)		300		300		300			1200	6.0
940117 (II)		180		180		180			600	4.5
940117 (III)		180		180		180			600	5.6
940117 (IV)		180				180				6.1
940202	900		300		300		600	600		3.0
940204 (I)	600		180		180		360	360		2.7
940204 (II)	600		180		180		360	360		2.1
940204 (III)	600		180		180		360	360		1.7
940204 (IV)	600		180		180		360	360		1.7
940205	2400		1200		1200		2400	2400		2.6
Total	5700	2220	2220	2040	2220	2220	4440	4440	6360	
m _{lim}	19.6	19.5	20.0	20.0	20.1	18.4	18.0	18.6	16.6	

Table 3 : Photometric Data

Filter Å	Num Stars	Num Obs	a	$\sigma(a)$	b	$\sigma(b)$	residual
3890	3	7	2.663	0.021	0.528	0.015	0.015
6075	3	7	1.662	0.017	0.207	0.012	0.007
7215	3	7	1.135	0.028	0.139	0.019	0.010
8480	3	7	3.404	0.056	0.065	0.038	0.015
9190	3	7	3.982	0.047	0.089	0.032	0.014
5795	4	4	1.644	0.031	0.285	0.020	0.013
6660	3	4	0.967	0.063	0.243	0.048	0.021
8020	4	4	2.300	0.025	0.116	0.014	0.006
9745	4	4	4.680	0.037	0.146	0.023	0.012

Table 4 : BATC Secondary Standard Stars in M67

ID	MMJ#	Sanders#	RA(2000)	DEC(2000)	3890	5795	6075	6660	7215	8020	8480	9190	9745
4118	6505	1288	8 51 42.36	11 51 22.87	13.449	11.103	10.887	10.676	10.609	10.596	10.465	10.341	10.316
3903	6504	1281	8 51 34.26	11 50 54.31	14.578	13.621	13.500	13.374	13.392	13.422	13.365	13.311	13.288
3751	5871	2223	8 51 29.86	11 51 29.76	14.060	13.250	13.132	13.025	13.055	13.097	13.053	12.985	12.973
3726	6503	1279	8 51 28.99	11 50 33.01	12.822	10.366	10.137	9.847	9.714	9.579	9.558
3347	6489	1054	8 51 17.05	11 50 46.26	13.342	10.977	10.765	10.549	10.424	10.459	10.338	10.213	10.173
3254	5559	2221	8 51 14.44	11 50 40.13	14.313	13.308	13.183	13.050	13.064	13.110	13.047	12.976	12.964
3202	5534	1052	8 51 12.68	11 50 34.43	14.567	13.558	13.424	13.307	13.315	13.334	13.294	13.227	13.208
3283	5573	1049	8 51 15.34	11 50 14.17	13.703	12.735	12.603	12.478	12.490	12.541	12.468	12.406	12.408
3659	3659	103	8 51 26.52	11 49 20.14	14.420	13.405	13.277	13.161	13.177	13.213	13.136	13.083	13.068
3607	5781	1027	8 51 24.95	11 49 0.65	14.226	13.169	13.036	12.914	12.927	12.958	12.882	12.827	12.811
3541	5739	1024	8 51 22.91	11 48 49.28	13.600	12.625	12.502	12.397	12.392	12.447	12.364	12.306	12.310
3668	6487	102	8 51 26.84	11 48 40.37	11.444	10.415	10.242	10.163	...	10.217	10.134	10.079	10.084
3717	5844	1011	8 51 28.70	11 48 2.04	14.868	13.718	13.575	13.437	13.434	13.437	13.357	13.281	13.259
3536	6485	1010	8 51 22.80	11 48 1.66	12.724	10.293	10.066	9.928	...	9.808	9.661	9.534	9.517
3349	6486	1016	8 51 17.10	11 48 16.01	12.971	10.087	9.750	9.463	9.317	9.177	9.124
3186	5522	1021	8 51 12.23	11 48 34.62	14.885	13.828	13.697	13.580	13.584	13.627	13.552	13.489	13.458
3755	6499	1250	8 51 29.91	11 47 16.78	12.565	9.433	...	8.912	8.547	8.403	8.375
3288	5571	1005	8 51 15.45	11 47 31.34	13.470	12.616	12.497	12.405	12.417	12.483	12.407	12.369	12.364
3267	5562	1003	8 51 14.76	11 47 23.87	13.738	12.759	12.624	12.520	12.521	12.570	12.495	12.437	12.433
3449	5667	997	8 51 19.91	11 47 0.32	12.834	12.071	11.942	11.869	11.880	11.957	11.890	11.853	11.834
3458	5675	2205	8 51 20.33	11 45 52.37	14.084	13.092	12.955	12.849	12.849	12.888	12.814	12.764	12.746
3465	5688	2204	8 51 20.57	11 46 16.31	13.608	12.843	12.732	12.653	12.679	12.745	12.683	12.653	12.633
3462	6483	988	8 51 20.55	11 46 4.74	14.155	13.114	12.973	12.857	12.865	12.909	12.834	12.777	12.778
3458	5678	2205	8 51 20.33	11 45 52.37	14.084	13.092	12.955	12.849	12.849	12.888	12.814	12.764	12.746
3380	5624	986	8 51 17.99	11 45 54.11	13.637	12.658	12.524	12.406	12.414	12.463	12.384	12.332	12.318
3805	5896	1234	8 51 31.24	11 45 50.54	13.538	12.549	12.415	12.306	12.300	12.357	12.267	12.214	12.218
3472	5695	976	8 51 20.81	11 45 2.39	14.096	13.017	12.883	12.766	12.760	12.806	12.730	12.681	12.661
3176	3176	977	8 51 11.78	11 45 22.05	9.835	10.096	10.048	10.148	...	10.500	10.471	10.480	10.526
3083	5464	990	8 51 8.64	11 46 11.71	14.325	13.362	13.227	13.122	13.133	13.171	13.087	13.052	13.025

Table 5 : Best Fit Isochrone of M67 in BATC Filter System

Mass (M_{\odot})	M_{3890}	M_{6075}	M_{7215}
0.52	11.95	8.71	8.31
0.57	11.39	8.22	7.84
0.63	10.83	7.77	7.42
0.67	10.24	7.35	7.03
0.71	9.64	6.96	6.68
0.75	9.04	6.59	6.35
0.79	8.46	6.25	6.04
0.83	7.90	5.91	5.73
0.87	7.34	5.57	5.42
0.92	6.77	5.21	5.09
0.98	6.21	4.84	4.74
1.04	5.64	4.44	4.35
1.11	5.05	3.98	3.92
1.20	4.49	3.47	3.41
1.23	4.08	3.12	3.08
1.26	3.88	2.84	2.78
1.28	3.89	2.73	2.65
1.29	4.23	2.77	2.65
1.30	4.99	3.03	2.85
1.31	4.81	2.53	2.32

Table 6 : Spatial Distribution of Stars within M67

type of star	m ₃₈₉₀	$\langle Mass \rangle$ M _⊙	Half-mass radius arcmin	half-mass radius pc
blue straggler		≥ 2.00	7.16 ± 2.13	1.63 ± 0.49
binary sequence	14.5 – 15.6	≤ 1.96	7.68 ± 2.07	1.75 ± 0.44
binary sequence	15.6 – 18.5	≤ 1.62	9.20 ± 1.69	2.10 ± 0.39
giant + subgiant		≥ 1.30	7.70 ± 0.84	1.75 ± 0.19
MS	13.8 – 14.5	≥ 1.20	10.23 ± 1.65	2.33 ± 0.38
MS	14.5 – 15.6	≥ 1.07	11.03 ± 1.18	2.51 ± 0.27
MS	15.6 – 18.5	≥ 0.87	11.81 ± 1.00	2.69 ± 0.23
MS b	15.6 – 18.5	≥ 0.87	12.00 ± 1.35	2.73 ± 0.31
MS r	15.6 – 18.5	≥ 0.87	11.29 ± 2.02	2.57 ± 0.46

Table 7 : Radial-Dependent Mass Function of M67

radius	η	total mass (no binary correction)	total mass (binary corrected)
arcsec		($M > 0.50M_{\odot}$)	($M > 0.50M_{\odot}$)
300	$+1.12 \pm 0.04$	218	272
500	$+0.76 \pm 0.28$	361	451
1000	$+0.01 \pm 0.07$	672	840
1500	-0.34 ± 0.08	931	1164
2000	-0.58 ± 0.14	1016	1270

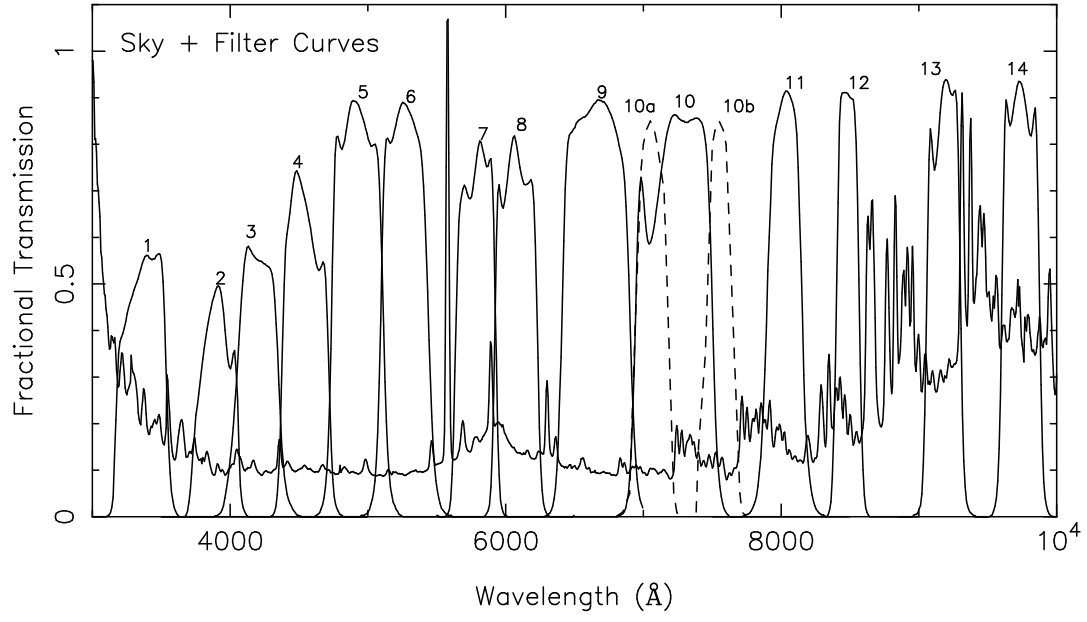


Fig 1. Fan et al.

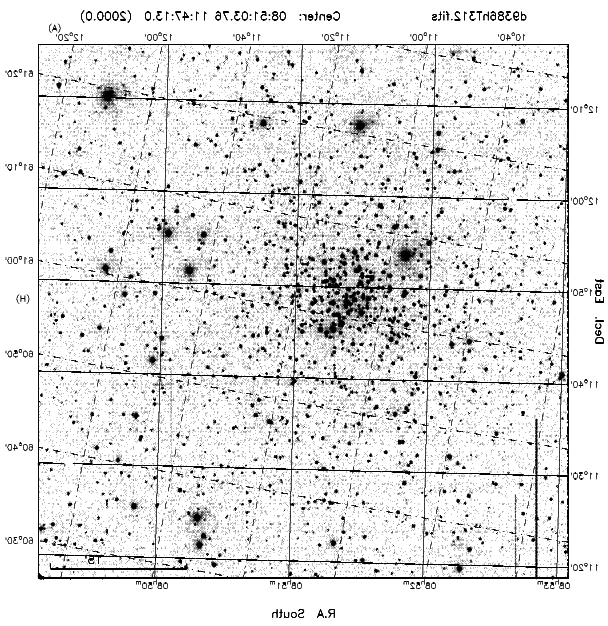


Fig 2. Fan et al.

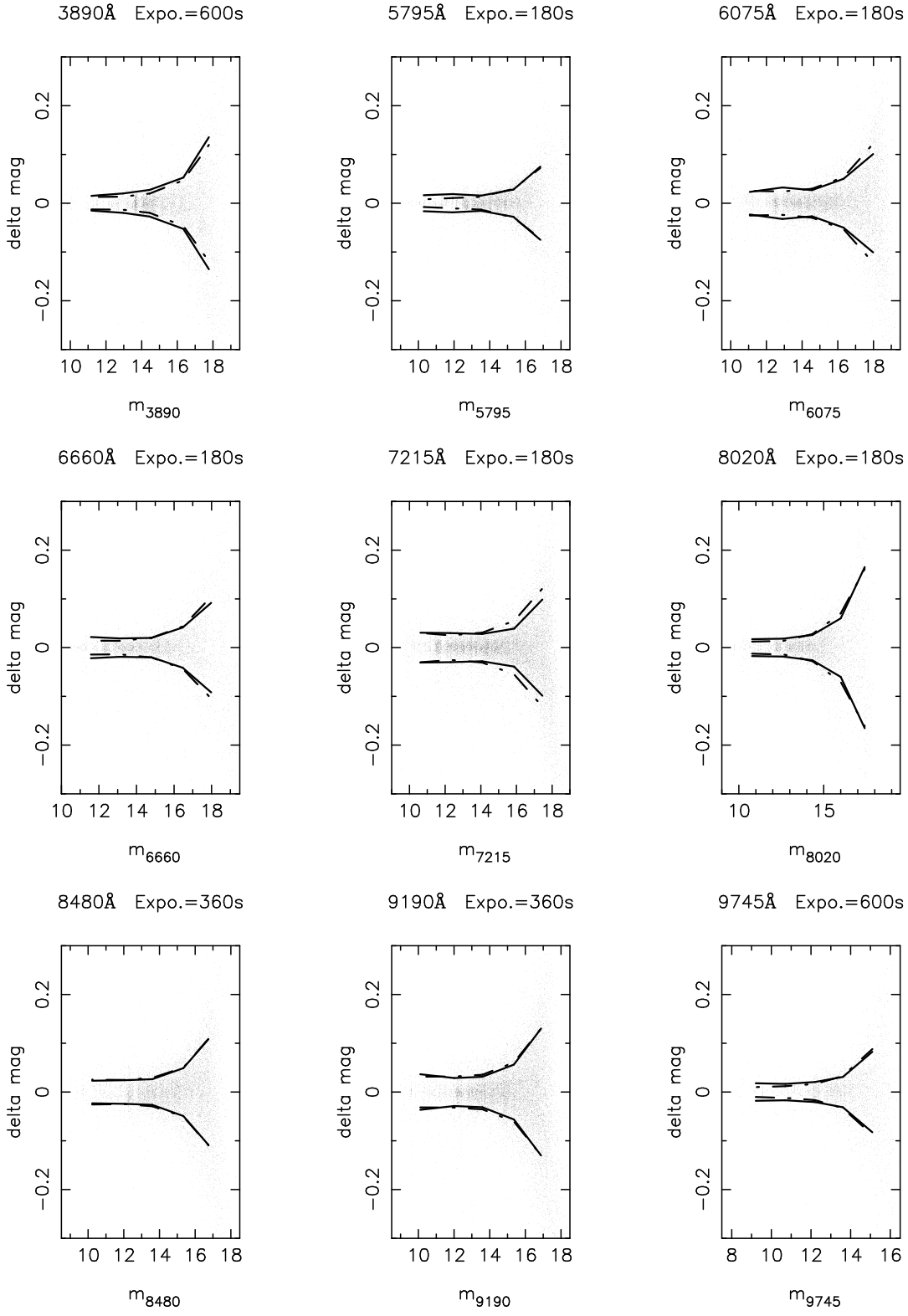


Fig 3. Fan et al.

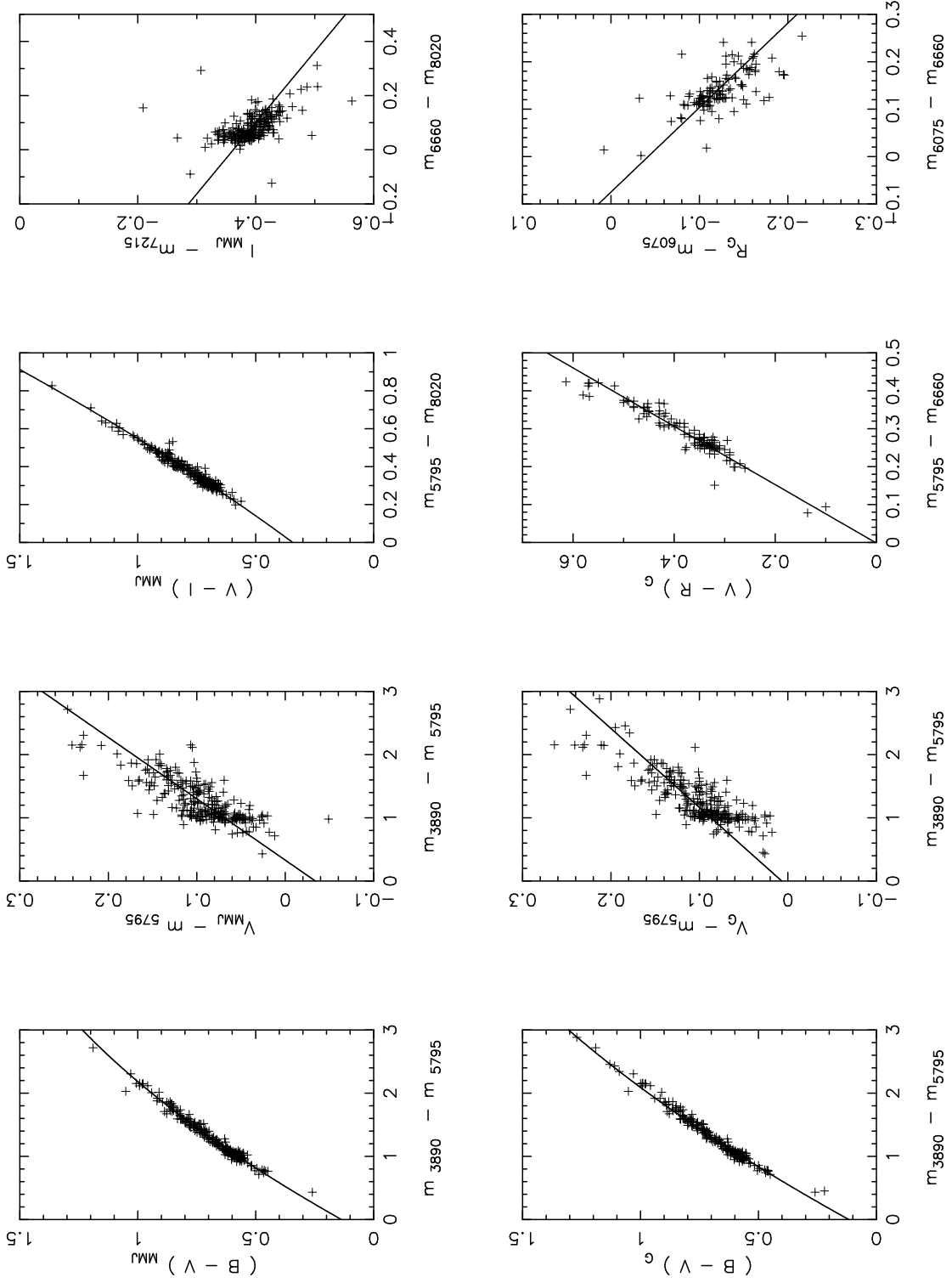


Fig 4. Fan et al.

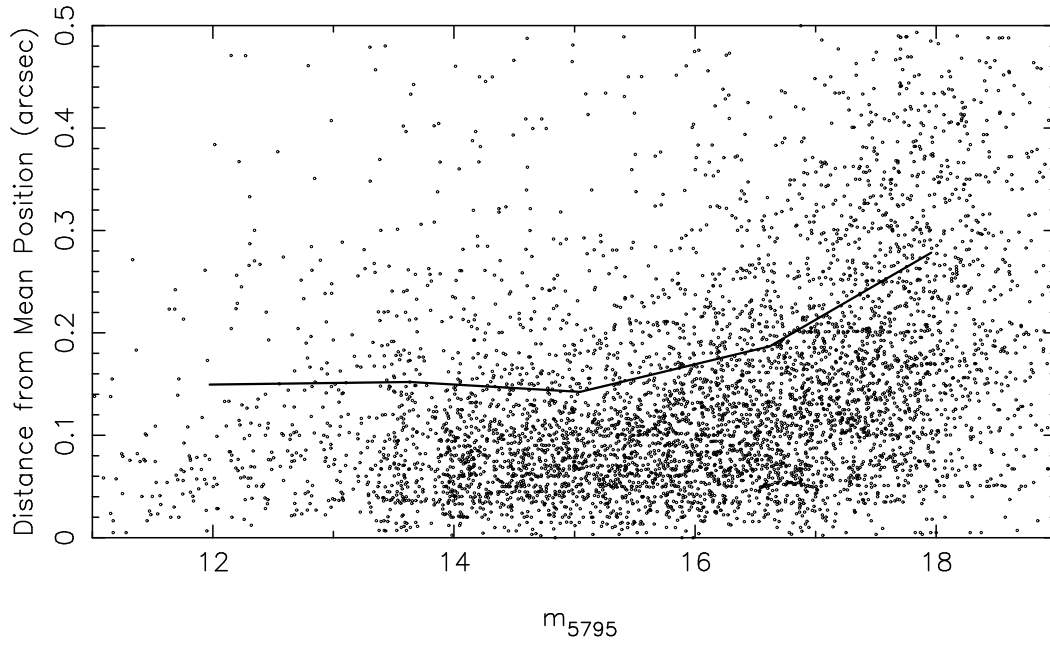


Fig 5. Fan et al.

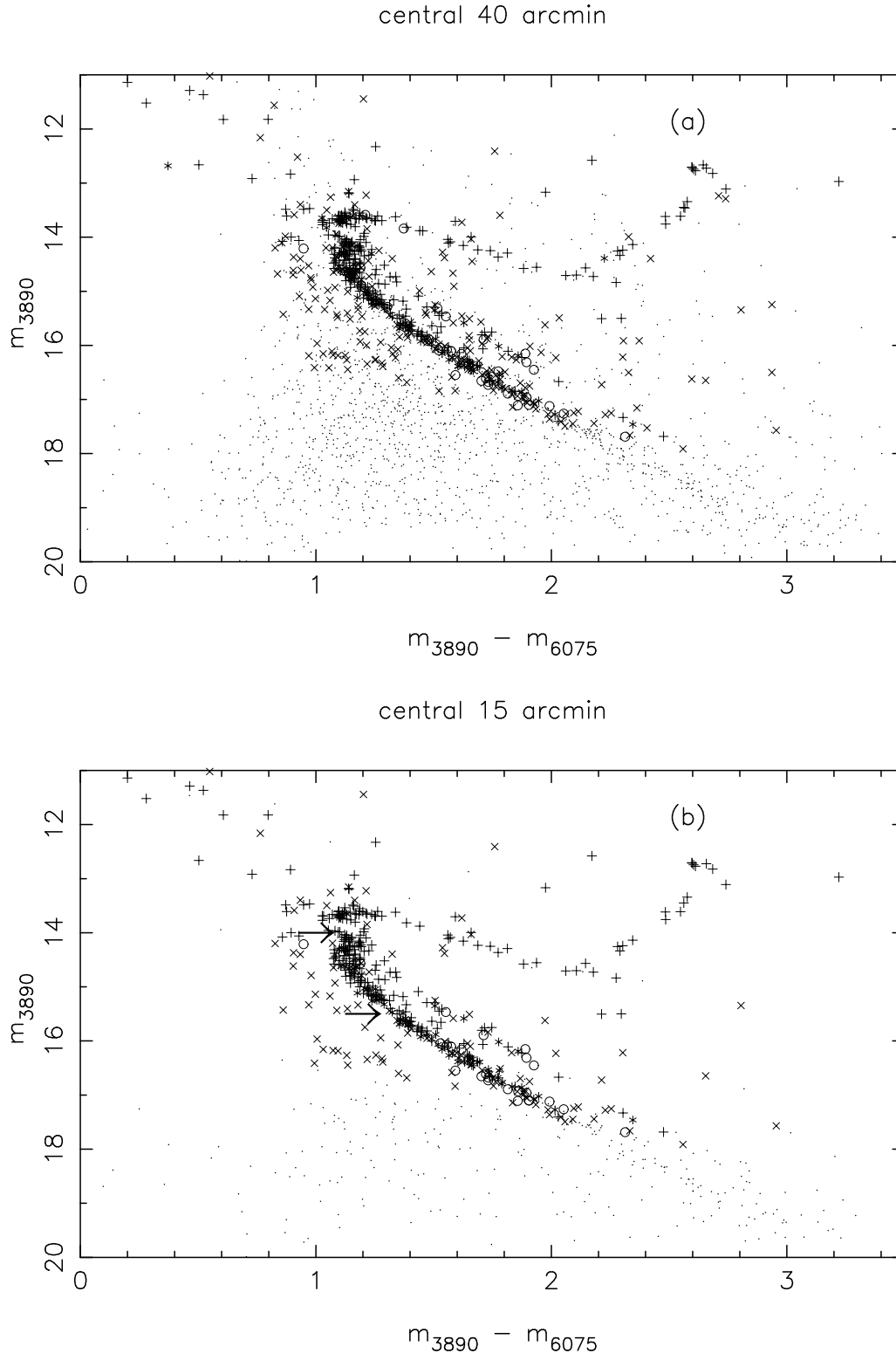


Fig 6. Fan et al.

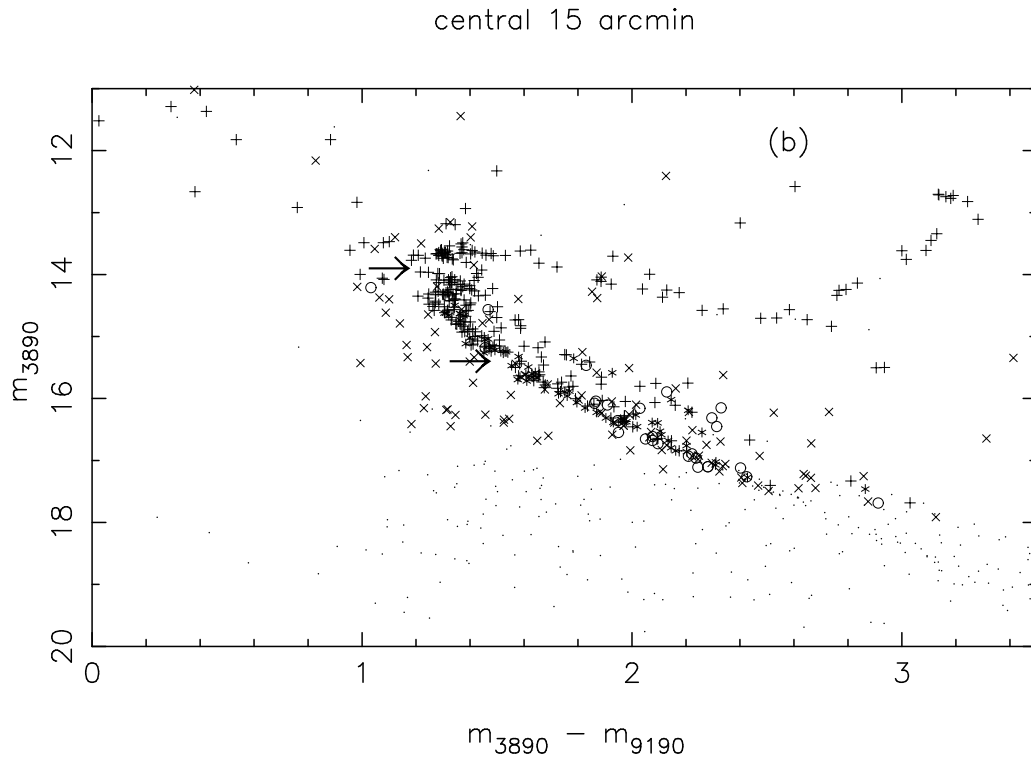
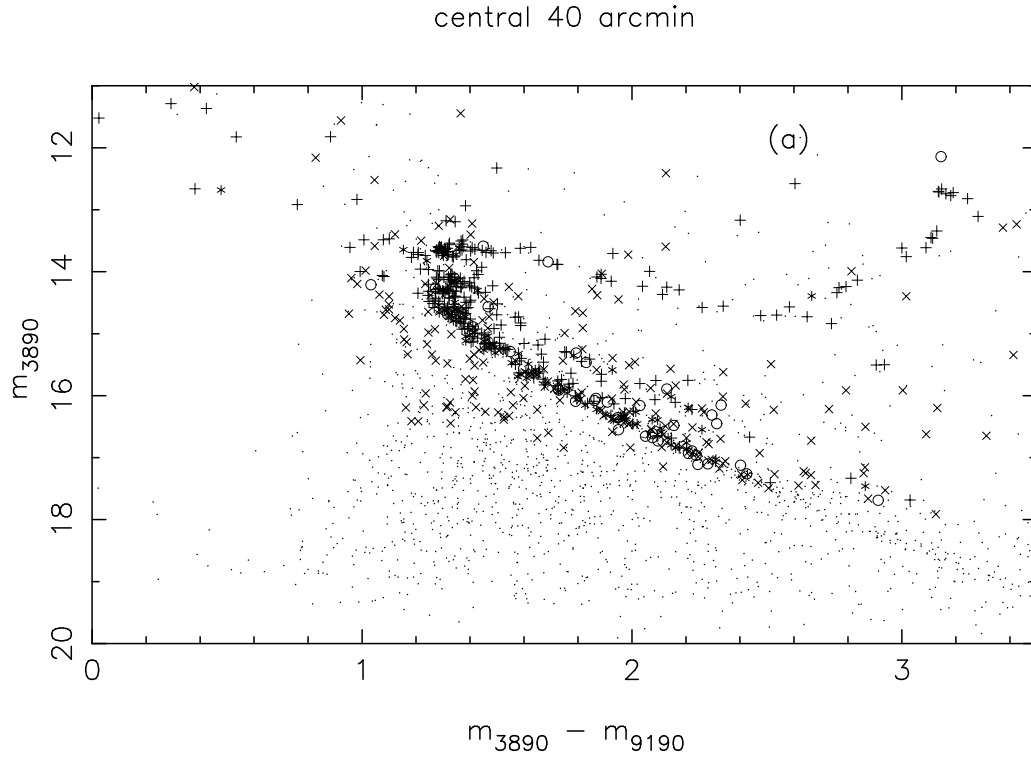


Fig 7. Fan et al.

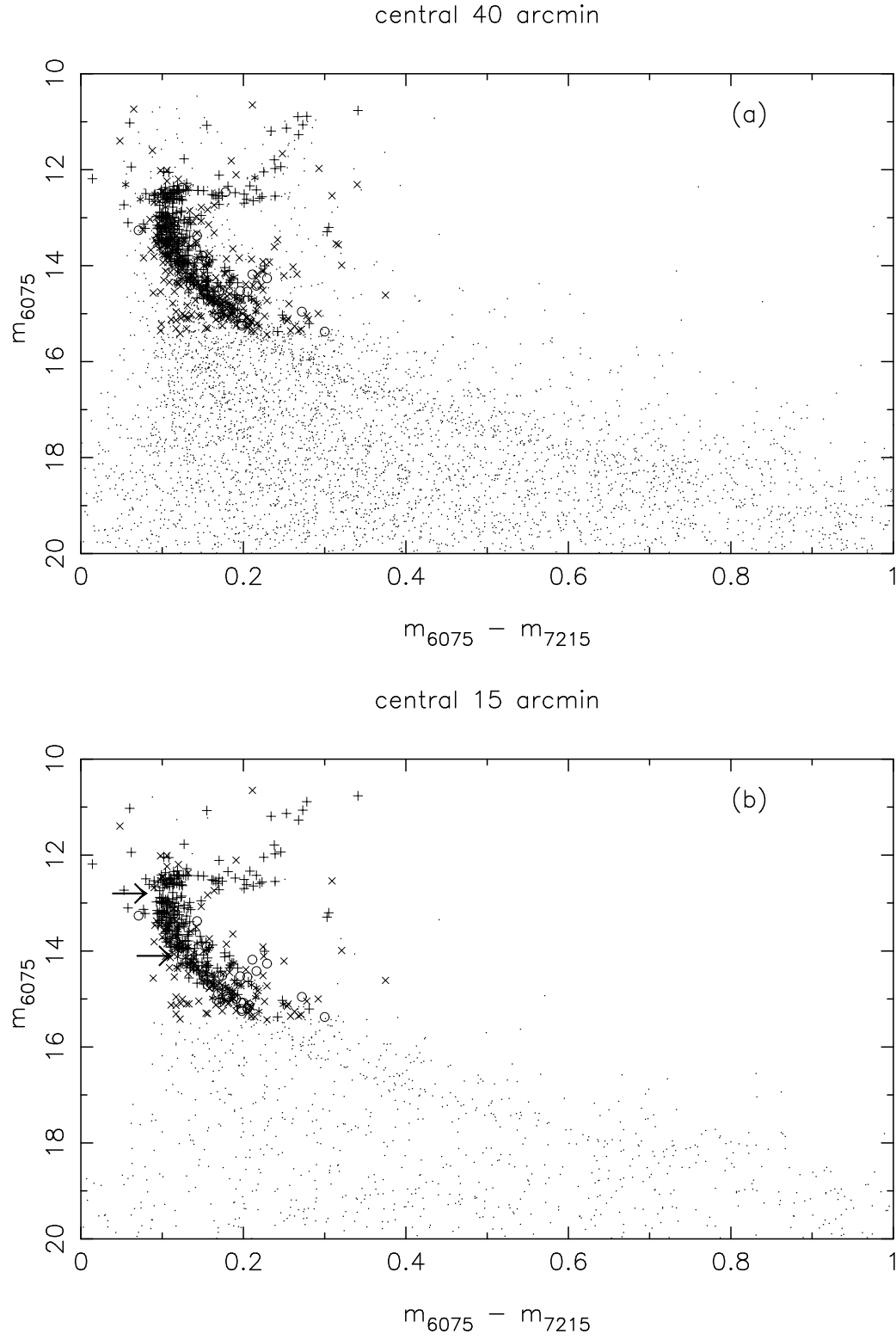


Fig 8. Fan et al.

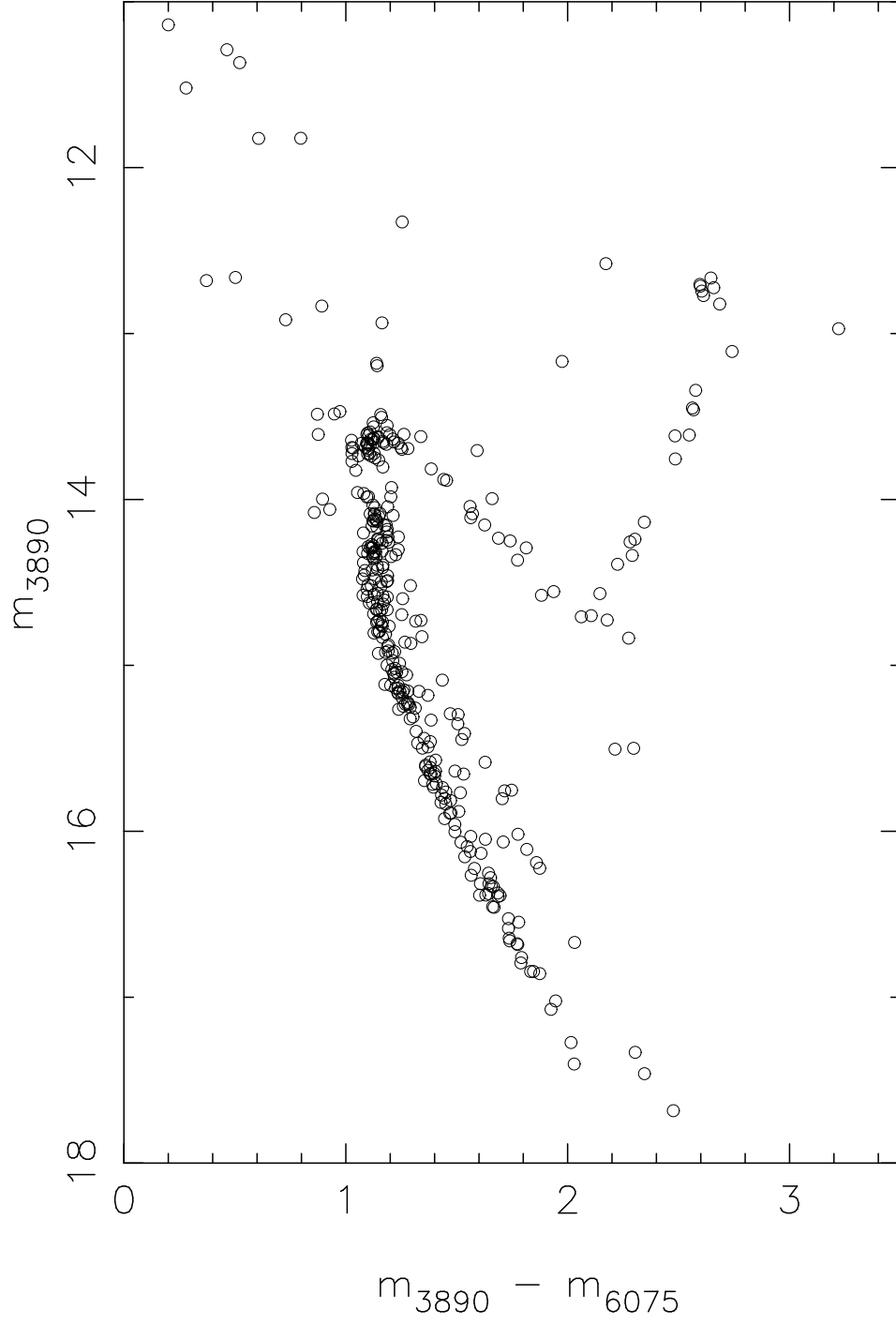


Fig 9. Fan et al.

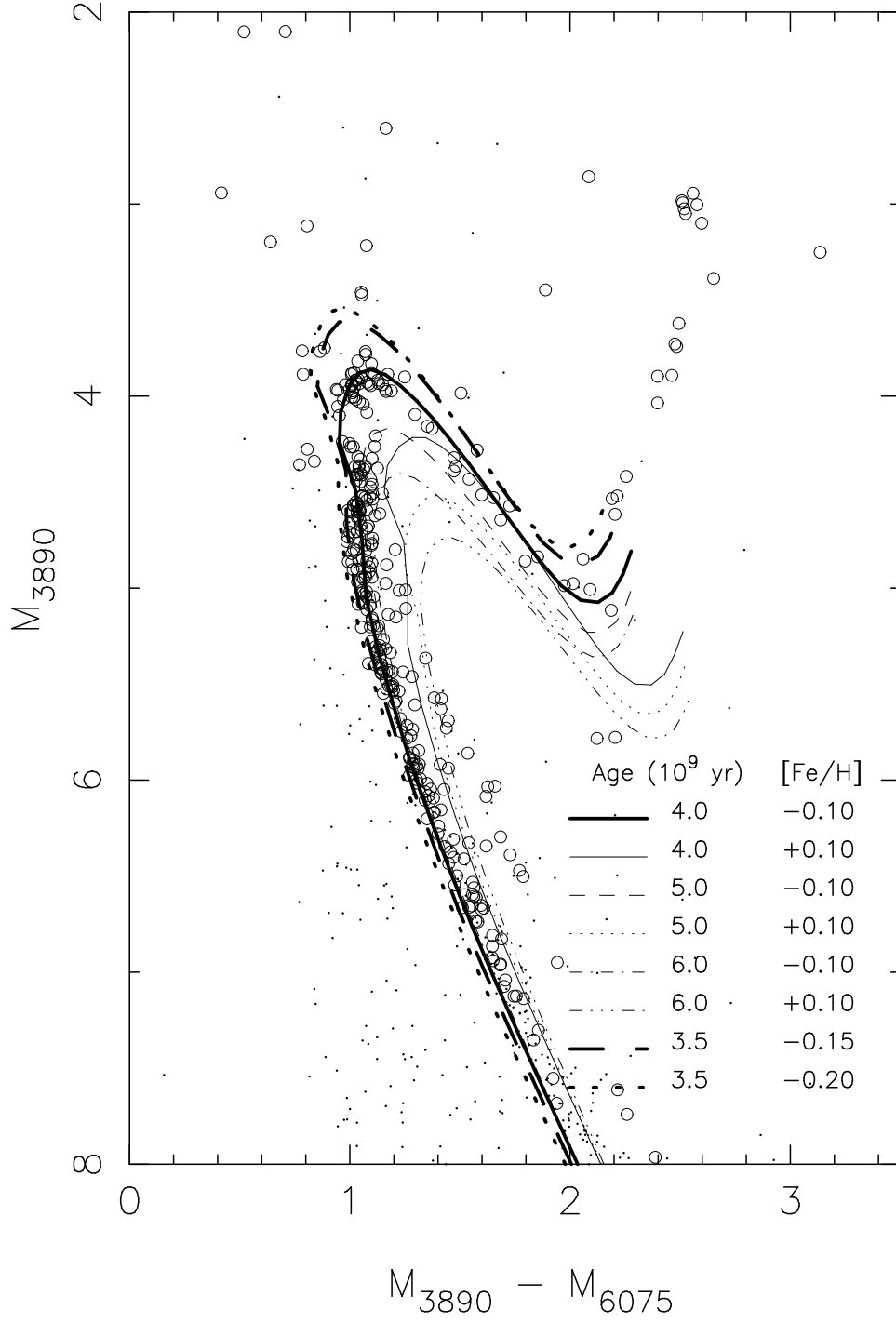


Fig 10. Fan et al.

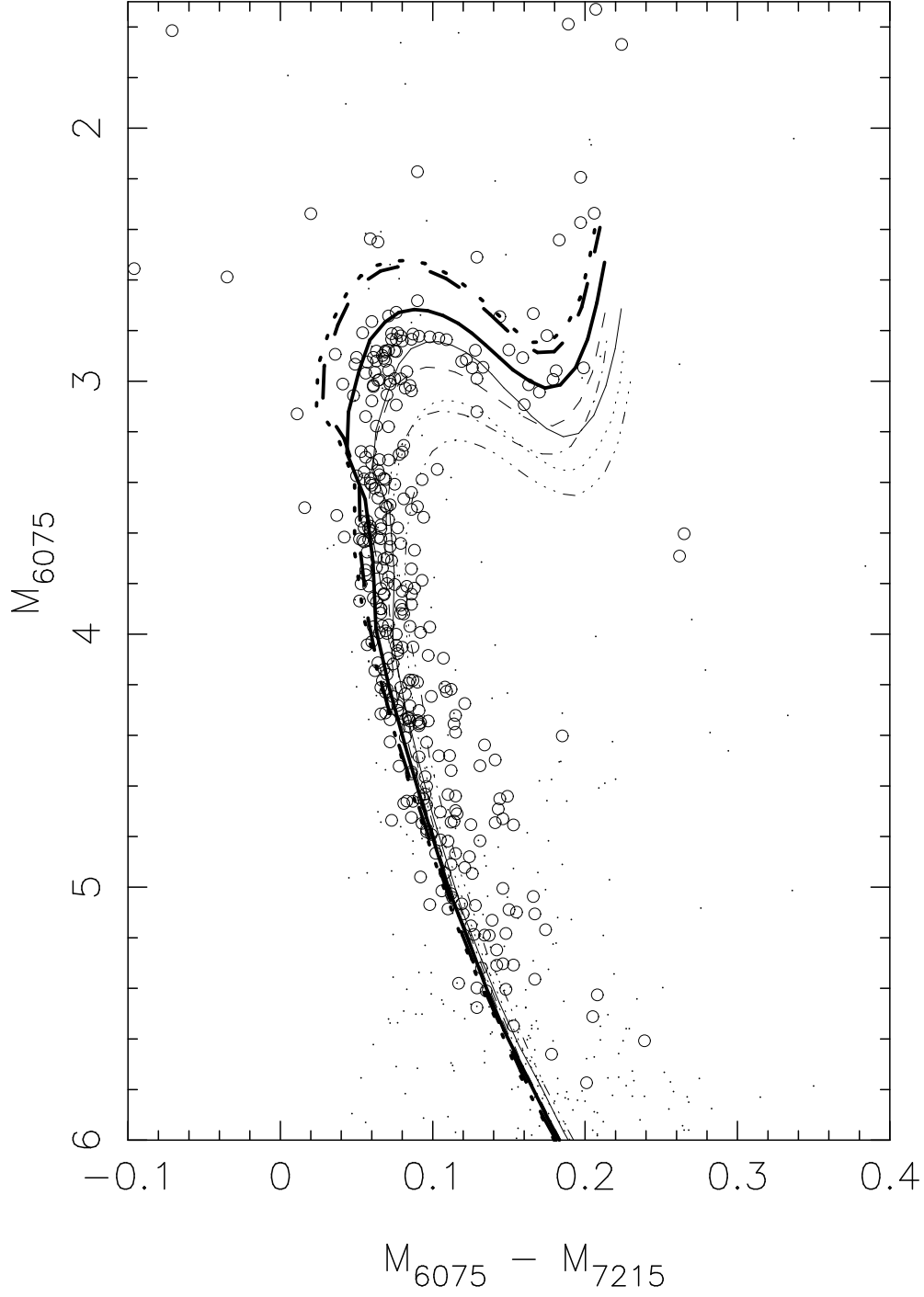


Fig 11. Fan et al.

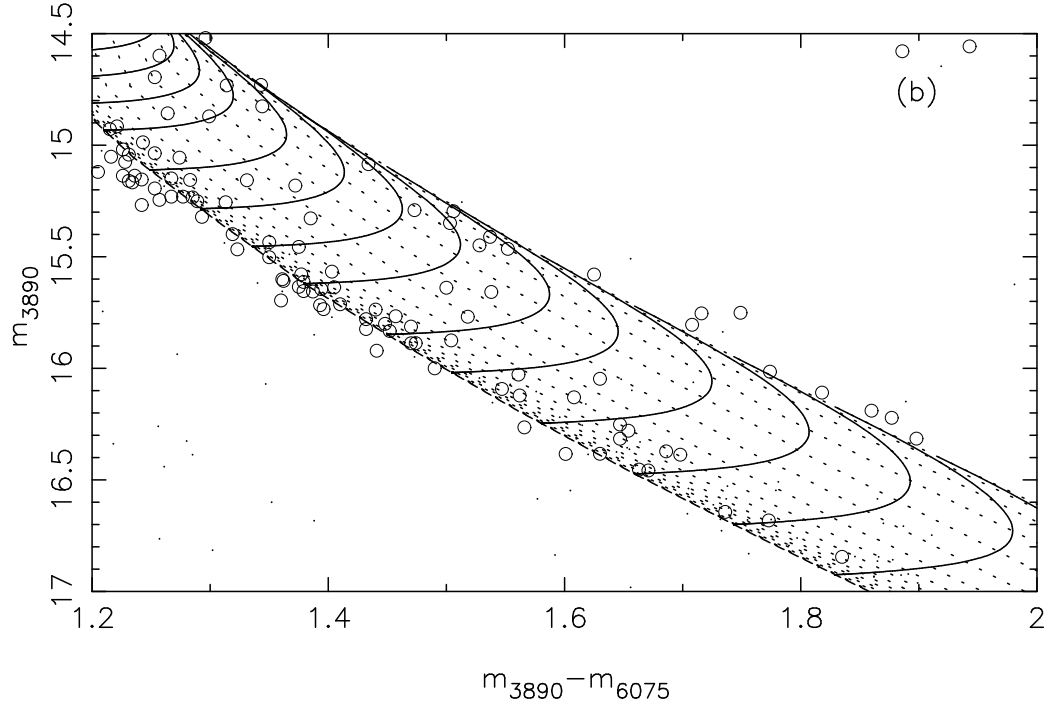
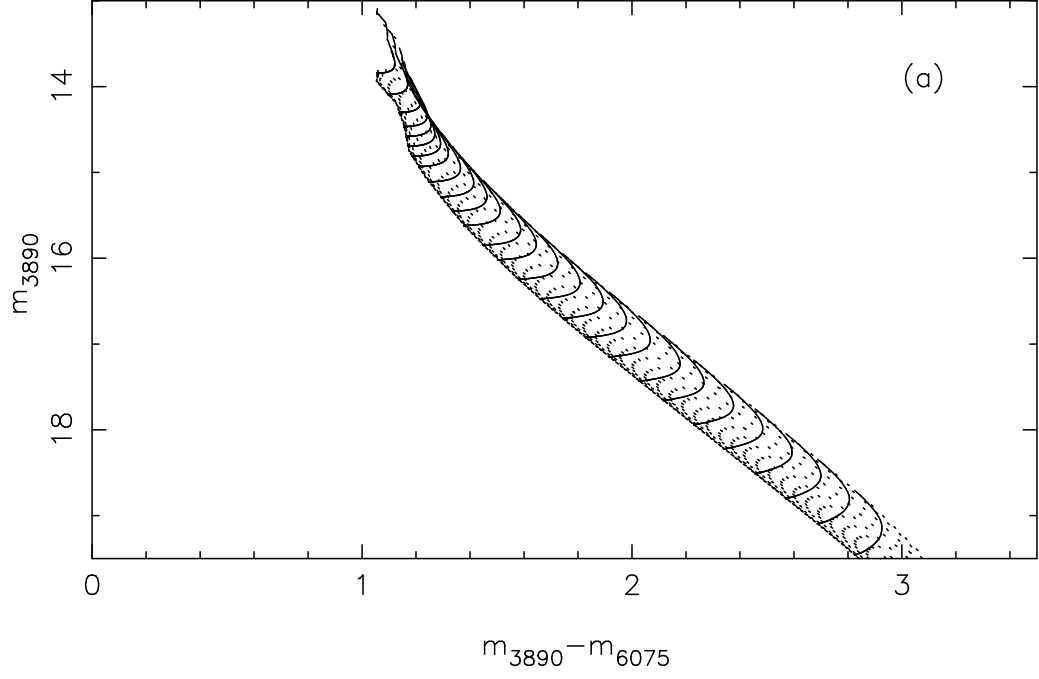


Fig 12. Fan et al.

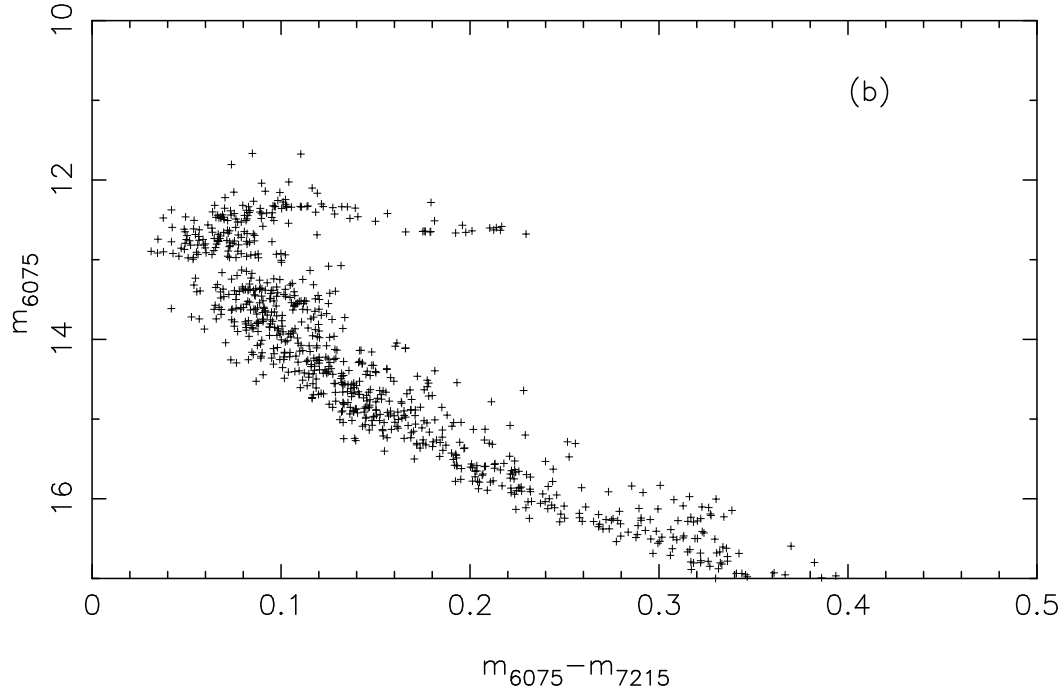
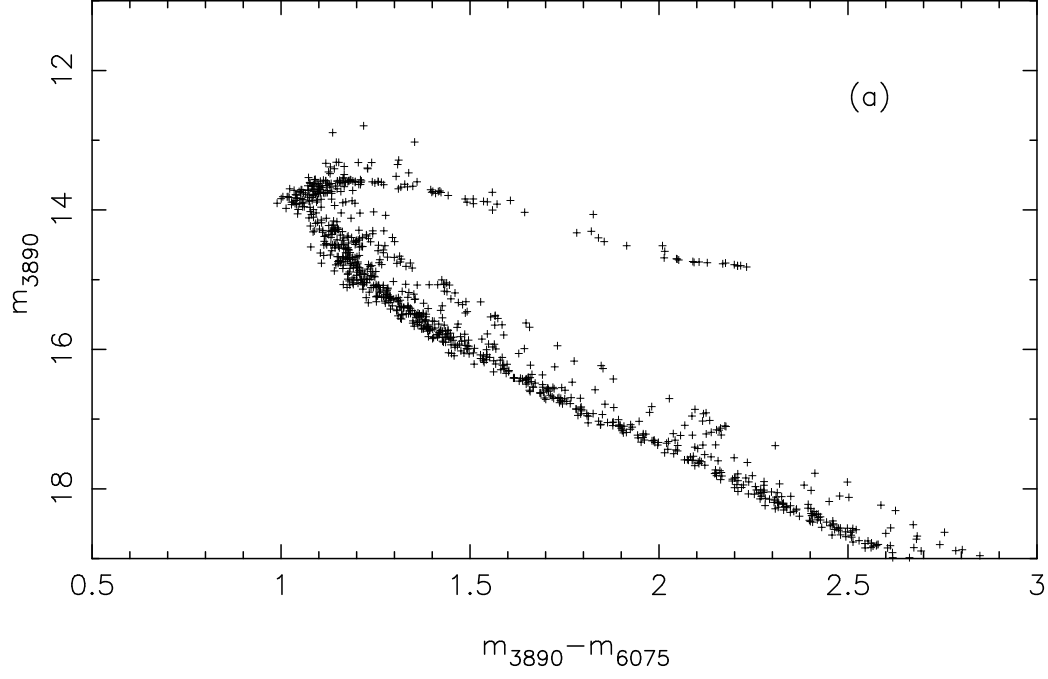


Fig 13. Fan et al.

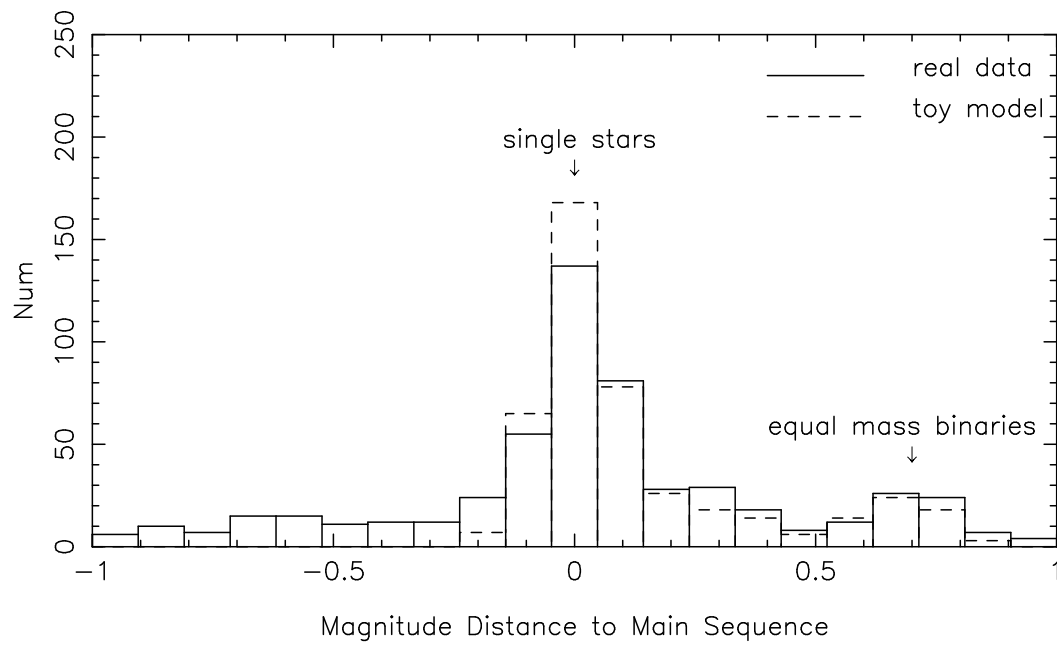


Fig 14. Fan et al.

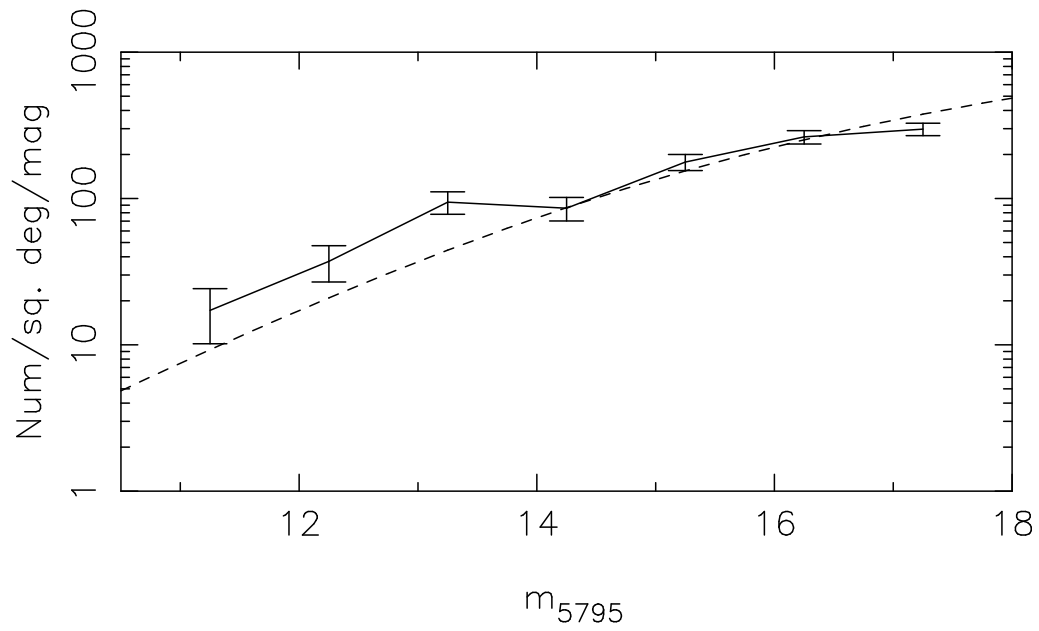


Fig 15. Fan et al.

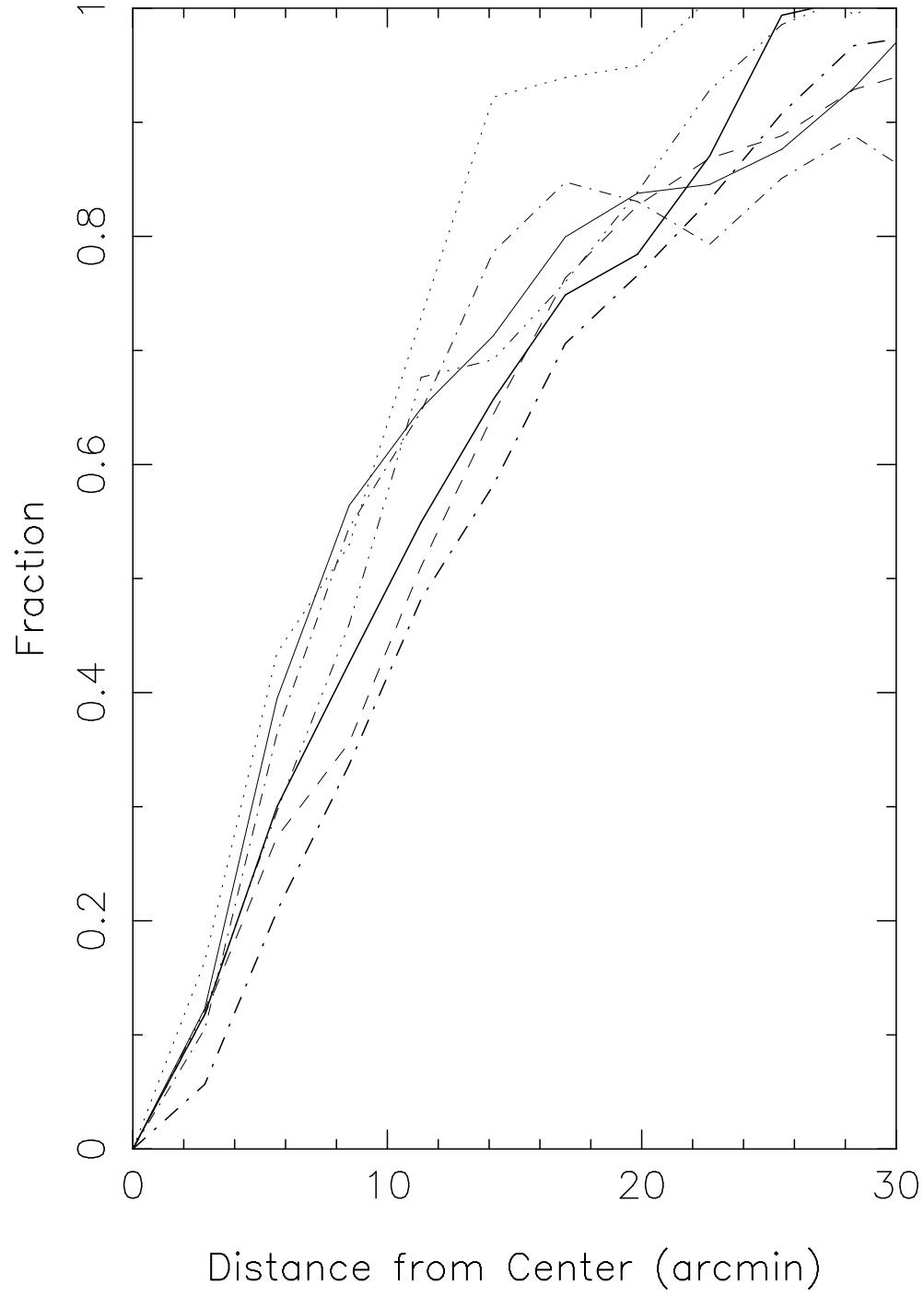


Fig 16. Fan et al.

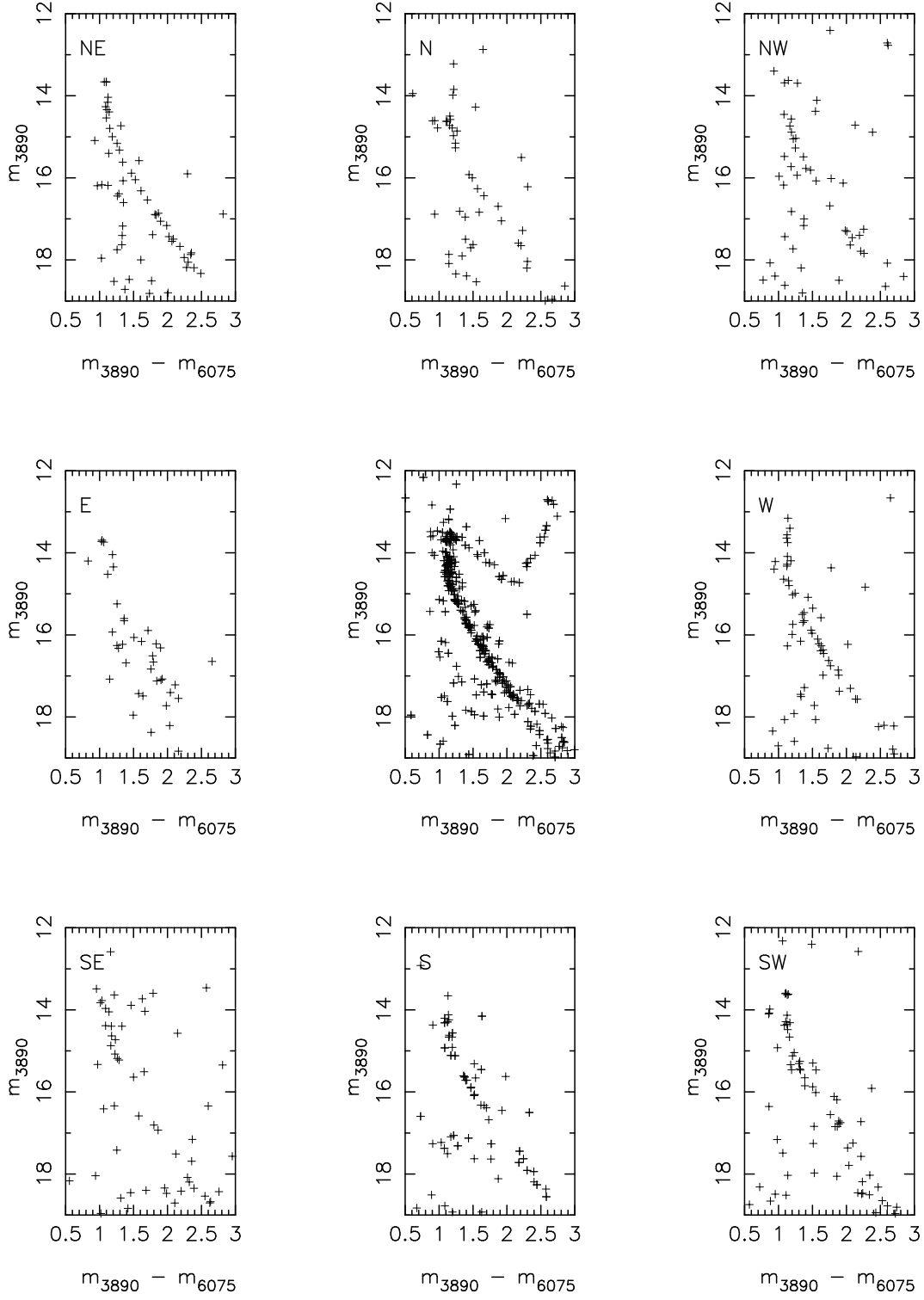


Fig 17. Fan et al.

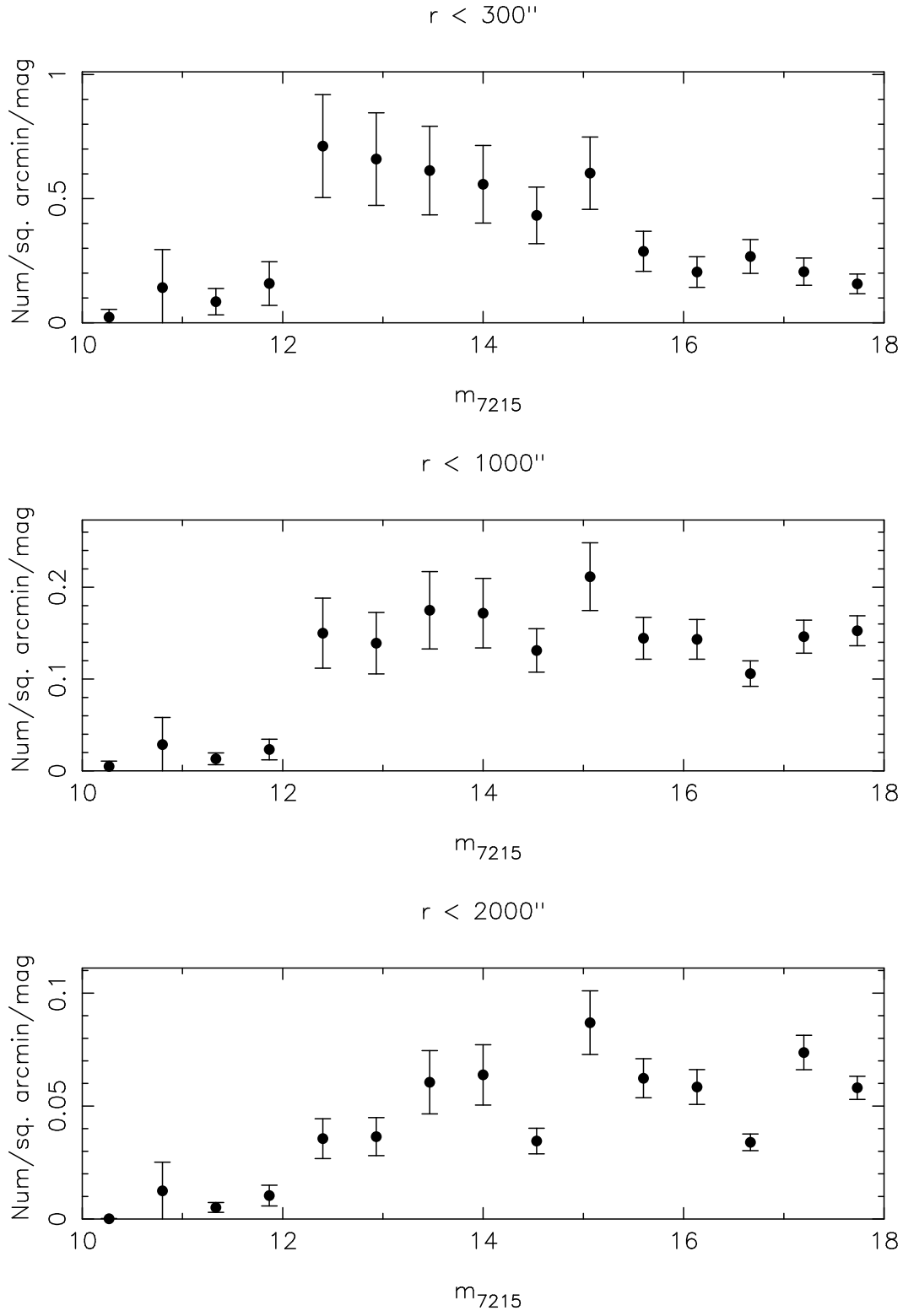


Fig 18. Fan et al.

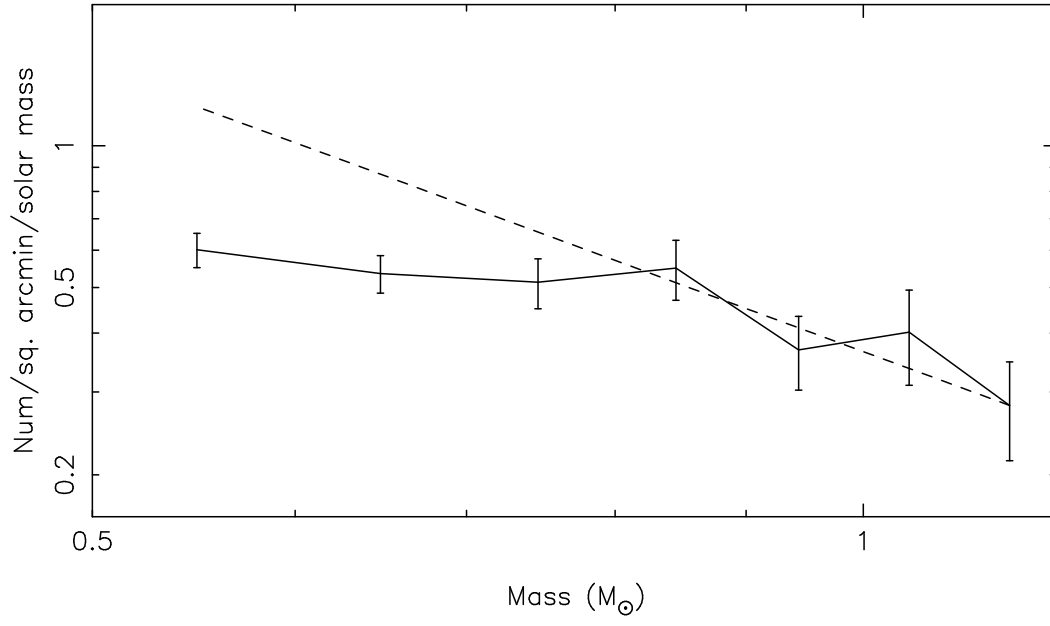


Fig 19. Fan et al.